Volume 59
Number 43
28 May 2023
Pages 6427–6598

ChemComm

Chemical Communications

rsc.li/chemcomm

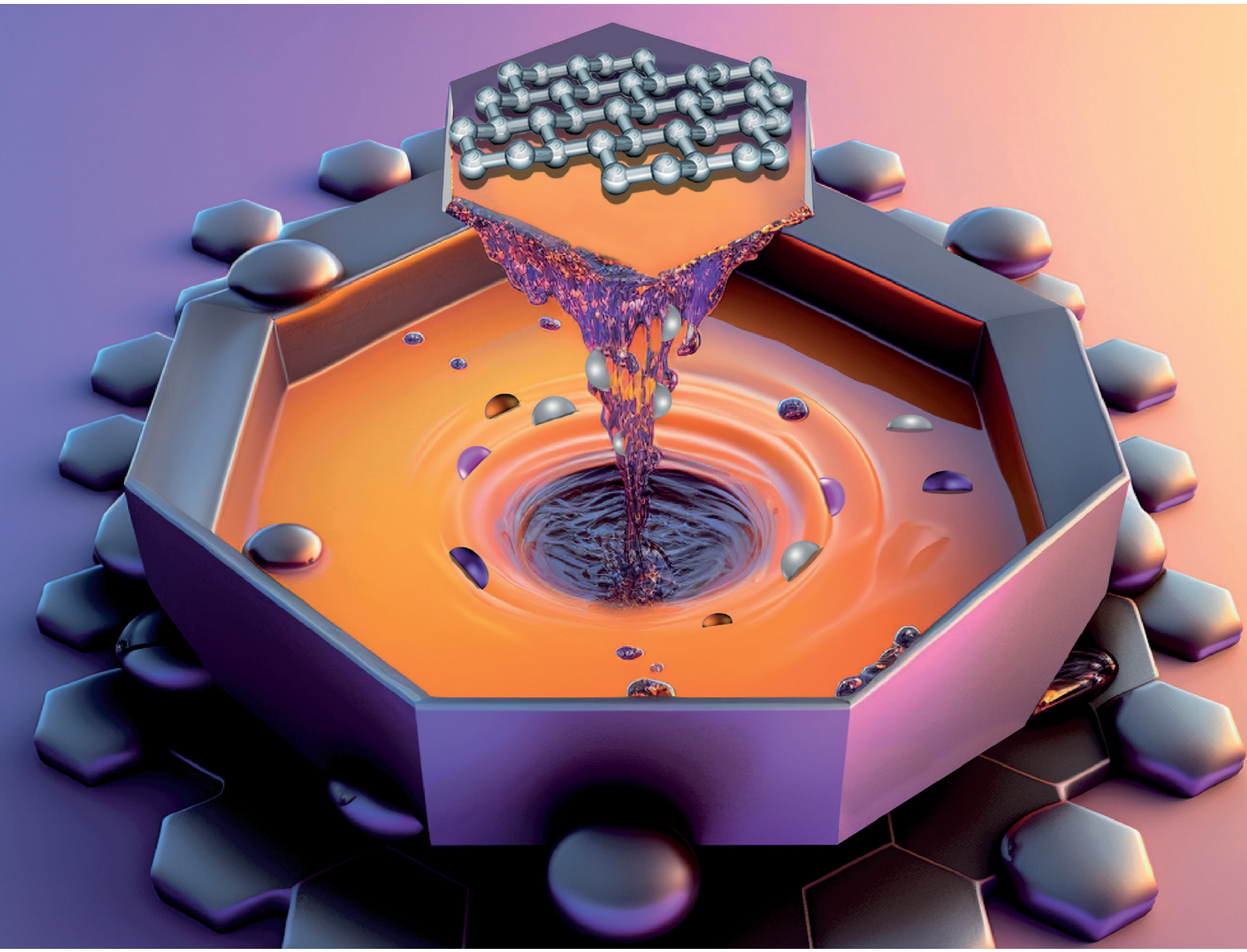

ISSN 1359-7345

ROYAL SOCIETY OF CHEMISTRY

FEATURE ARTICLE

Gonzalo Abellán *et al.*

Chemistry of two-dimensional pnictogens: emerging post-graphene materials for advanced applications

ChemComm

FEATURE ARTICLE

View Article Online
View Journal | View Issue

Open Access Article. Published on 21 April 2023. Downloaded on 5/10/2026 2:30:36 PM.
This article is licensed under a Creative Commons Attribution-NonCommercial 3.0 Unported Licence.

Check for updates

Cite this: *Chem. Commun.*, 2023, **59**, 6453

Chemistry of two-dimensional pnictogens: emerging post-graphene materials for advanced applications

Matteo Andrea Lucherelli,† Víctor Oestreicher,† Marta Alcaraz and Gonzalo Abellán *

The layered allotropes of group 15 (P, As, Sb and Bi), also called two-dimensional (2D) pnictogens, have emerged as one of the most promising families of post-graphene 2D-materials. This is mainly due to the great variety of properties they exhibit, including layer-dependent bandgap, high charge-carrier mobility and current on/off ratios, strong spin–orbit coupling, wide allotropic diversity and pronounced chemical reactivity. These are key ingredients for exciting applications in (opto)electronics, heterogeneous catalysis, nanomedicine or energy storage and conversion, to name a few. However, there are still many challenges to overcome in order to fully understand their properties and bring them to real applications. As a matter of fact, due to their strong interlayer interactions, the mechanical exfoliation (top-down) of heavy pnictogens (Sb & Bi) is unsatisfactory, requiring the development of new methodologies for the isolation of single layers and the scalable production of high-quality flakes. Moreover, due to their pronounced chemical reactivity, it is necessary to develop passivation strategies, thus preventing environmental degradation, as in the case of bP, or controlling surface oxidation, with the corresponding modification of the interfacial and electronic properties. In this Feature Article we will discuss, among others, the most important contributions carried out in our group, including new liquid phase exfoliation (LPE) processes, bottom-up colloidal approaches, the preparation of intercalation compounds, innovative non-covalent and covalent functionalization protocols or novel concepts for potential applications in catalysis, electronics, photonics, biomedicine or energy storage and conversion. The past years have seen the birth of the chemistry of pnictogens at the nanoscale, and this review intends to highlight the importance of the chemical approach in the successful development of routes to synthesise, passivate, modify, or process these materials, paving the way for their use in applications of great societal impact.

Received 23rd November 2022,
Accepted 2nd March 2023

DOI: 10.1039/d2cc06337a

rsc.li/chemcomm

1. Introduction

The discovery of graphene at the beginning of this century[1] has led to the development of research on two-dimensional (2D) materials, giving rise to a range of different layered materials with exciting properties that can be applied in fields such as optoelectronics, energy conversion and storage,[2] catalysis,[3] biosensors,[4] or drug delivery,[5] to name a few. The conventional production approaches encompass top-down and bottom-up routes like micromechanical (μME) and liquid phase exfoliation (LPE),[6] chemical vapour deposition (CVD) or pure wet-chemical direct synthetic methods.[7] These methodologies have been successfully used for the preparation of several transition-metal dichalcogenides (TMD), transition metal phosphides, nitrides and carbides, layered hydroxides, layered oxides, perovskites, 2D covalent-organic-frameworks, 2D-coordination polymers or Mxenes.[8] Among these, the number of examples of monoelemental 2D materials is much scarcer. Of special interest are the elemental materials of group 15 of the Periodic Table, the so-called pnictogens, constituted by the natural elements: nitrogen, phosphorus, arsenic, antimony and bismuth, the so-called 2D-Pnictogens (2D-Pn).[9] The origin of the name pnictogens, which can be translated as "suffocator maker" –according to the suggestion of Dutch chemist Anton Eduard van Arkel (1893–1976) in the early 1950s– came from the Greek root word "*pnikta*", which means "suffocated things", mainly due to inability of gaseous nitrogen to support life or combustion, which in German is Stickstoff, or "suffocating substance", but also extended to phosphorus compounds which, in aquatic ecosystems, might have an indirect suffocating effect on aquatic life by inducing the overgrowth of bacterias.[10]

Instituto de Ciencia Molecular (ICMol), Universidad de Valencia, Catedrático José Beltrán, 46980, Paterna, Valencia, Spain. E-mail: gonzalo.abellan@uv.es
† These authors contributed equally to this work.

Open Access Article. Published on 21 April 2023. Downloaded on 5/10/2026 2:30:36 PM.
This article is licensed under a Creative Commons Attribution-NonCommercial 3.0 Unported Licence.

2D-Pn materials have witnessed increasing attention because their properties can meet the limitations of graphene, such as the absence of band-gap or the pronounced chemical inertness, features that, for example, have precluded the development of highly efficient electronic micro-devices. For this reason, semiconducting 2D black phosphorus (bP) has emerged as a promising alternative to fill this gap.[2] Moreover, 2D-Pn exhibit a great variety of physical properties like tunable layer-dependent bandgap, ballistic transport, or strong spin–orbit coupling, to name a few, thus making these materials very promising for (opto)electronic applications, like solar cells or field effect transistors (FET) as well as for spintronic devices.[9] Moreover, from a chemical point of view, 2D-Pn are also particularly appealing due to their monoelemental nature (which simplifies its study), their high specific- and volumetric-capacities when used as electrode materials for energy storage systems, or their excellent behaviour as heterogeneous catalysts.[11] Altogether, 2D-Pn exhibits a wide range of physical and chemical properties that can be exploited in different applications of great social importance, however,

Matteo Andrea Lucherelli

Matteo Andrea Lucherelli obtained his PhD in Therapeutic Chemistry and Biochemistry in 2019 at the University of Strasbourg. His thesis was aimed at the development of graphene-based multifunctional materials and 2D materials for biomedical applications. He worked in the development of biobased polymers before moving to the University of Valencia, awarded as APOSTD fellow postdoctoral researcher. Currently, his research is focused on the development of 2D pnictogens materials and their intercalation's compounds for biomedical and energy applications. His interests spread from nanomedicine to energy storage applications, with an organic chemistry approach to the nanomaterial's world.

Víctor Oestreicher

Víctor Oestreicher studied chemistry and obtained his PhD at the University of Buenos Aires. His thesis, supervised by Matías Jobbágy, was focused on the development of a new synthetic approach for the obtaining of inorganic and hybrid materials such as layered hydroxides, hydrogels, MOFs and phosphates: the epoxide route. After that, he worked on an industrial project led by Galo Soler-Illia and Paula Angelomé centred on the development of a new colloidal synthesis compatible with gold recovery. His current research interests are focused on the synthesis of 2D-hybrid materials using a colloidal approach as well as on the development of straightforward and scalable synthetic methods for electroactive materials for energy storage and conversion.

Marta Alcaraz

Marta Alcaraz received her degree in Chemistry in 2018 from the University of Granada (Spain). She completed her Master's thesis in Organic Chemistry at the University of Valencia in 2019. Afterwards, she began her PhD in Nanoscience and Nanotechnology, focusing on the synthesis of 2D-pnictogens from a colloidal chemistry point of view, aimed to control the interface of these novel nanomaterials.

Gonzalo Abellán

Gonzalo Abellán obtained his PhD in Nanoscience and Nanotechnology in 2014 at the University of Valencia (UV). Afterwards, he gained a self-driven Marie Curie Fellowship and joined Prof. Andreas Hirsch's group at the Friedrich-Alexander-Universität, Erlangen-Nürnberg. In 2018 he returned to Spain as an Excellence Distinguished Researcher getting a GenT-CIDEGENT contract (Generalitat Valenciana), the Ramón y Cajal fellowship, the ERC Starting Grant, or the ERC Proof of Concept Grant, among others. Gonzalo Abellán's main research activities have been focused on three lines: 2D-pnictogens (group of P, As, Sb and Bi), layered hydroxides, and carbon nanoforms and related hybrid materials, with special emphasis on energy-related applications. He leads the 2D-Chem research group at the Institute of Molecular Science (ICMol, UV).

 This journal is © The Royal Society of Chemistry 2023

Open Access Article. Published on 21 April 2023. Downloaded on 5/10/2026 2:30:36 PM.
This article is licensed under a Creative Commons Attribution-NonCommercial 3.0 Unported Licence.

several challenges related to its stability, processing or large-scale production must be overcome.

Before guiding the readers to the nanoscale properties of 2D-Pn, is it worth recalling their elemental bulk properties keeping in mind to better trace the current research development. Their first classification from the Periodic Table suggests a marked difference between them, with N and P belonging to non-metals elements, while As and Sb are considered metalloids and Bi a metal. These last three members are commonly known as heavy pnictogens. Elemental nitrogen is the only one that exists as a molecular gas under environmental conditions, N_2. In the case of phosphorus, a wide variety of allotropes can be found, ranging from molecular to extended solids. Specifically, white phosphorus is an air-sensitive molecular solid composed of P_4 entities.

Among the extended phases, while the red phosphorus is an amorphous polymeric solid, the violet, black and blue phosphorus are crystalline structures, being bP the most stable one. It is worth noting that black and blue phosphorus are layered structures, also known as α and β structures, respectively. Analogously, arsenic also can be found as a molecular solid (As_4, more stable than white phosphorus), showing both α- and β-layered structures. Finally, antimony and bismuth elements are mainly found as extended crystalline solids, being the β form the most stable one.[9]

Concerning their layered structures, α-form exhibits an orthorhombic disposition where the atoms are arranged in a six-member rings pucked structure (Fig. 1A), while the β-form displays a rhombohedral structure (Fig. 1B). Indeed, bP's will be mainly found in its α-form, while the other Pn members exhibit the β-one. Additionally, the α and β structures affect the bulk nature of their allotropes, as in the case of the heavier 2D-Pn that are characterised by strong interlayer interactions (higher than in graphene) increasing from As to Bi, associated with the corresponding increment of their metallic character.[9,12] This aspect is crucial for 2D-Pn production, which we will further discuss below.

From the chemical point of view, tabulated redox potentials give a straightforward idea of the chemical reactivity in terms of the redox reactions for bulk Pn, which can be easily visualised in a Frost diagram (for sake of clarity N has been avoided).[14] As depicted in Fig. 2, and calculated under acidic aqueous conditions, negative oxidation states are available for all the Pn members. In the case of the oxidation state (−3), the reducing strength decreases from P to Bi in comparison with the zero valent species. In the case of the highest oxidation state (+5), all the Pn have positive reduction potential except P, showing its particularly high tendency towards oxidation. Since Frost diagrams are based on reduction potentials measured in aqueous solution, this can be considered as a first input pointing out the

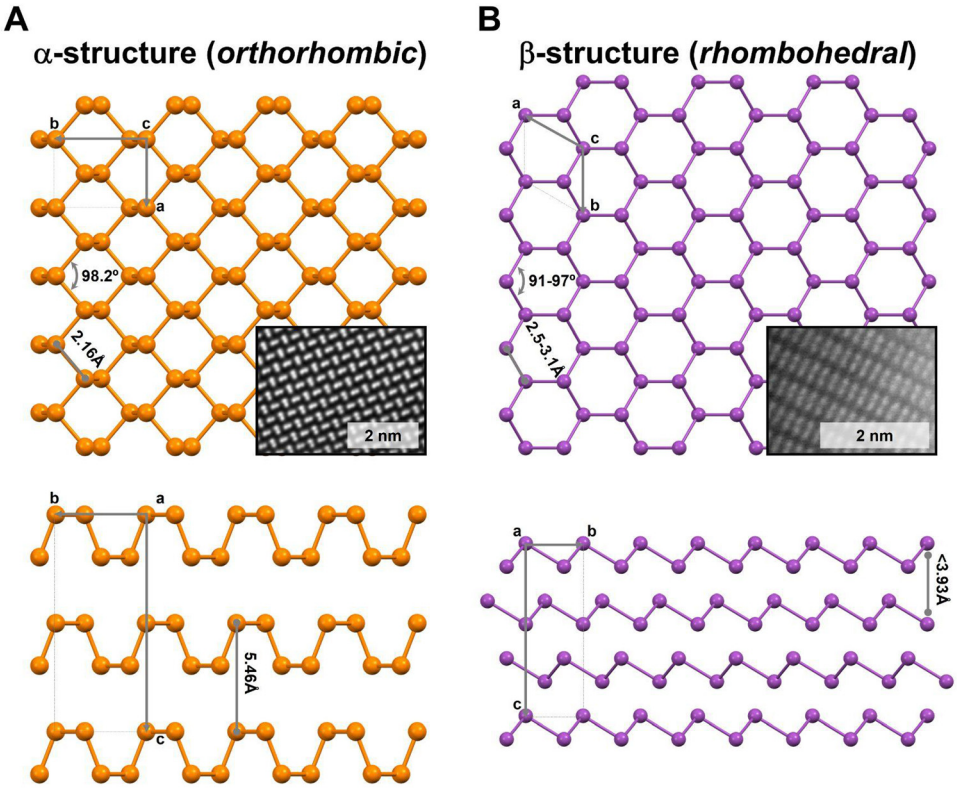

Fig. 1 Schematic representation of α- and β-layered structures of Pn. (A) Top and side views of the orthorhombic structure (*Cmce* space group), corresponding to the most stable thermodynamic form of P as bP. (B) Top and side views of the rhombohedral structure (*R3m* space group), corresponding to the most stable thermodynamic form of As, Sb and Bi. The insets show aberration-corrected STEM atomic-resolution HAADF images (not corresponding with the orientation shown in the crystal structure sketches) measured at 80 kV of 2D-α-BP (Fourier filtered) and 2D-β-Sb, respectively.[11,13] Characteristic distances and angles according to the crystal structure.

Open Access Article. Published on 21 April 2023. Downloaded on 5/10/2026 2:30:36 PM.
This article is licensed under a Creative Commons Attribution-NonCommercial 3.0 Unported Licence.

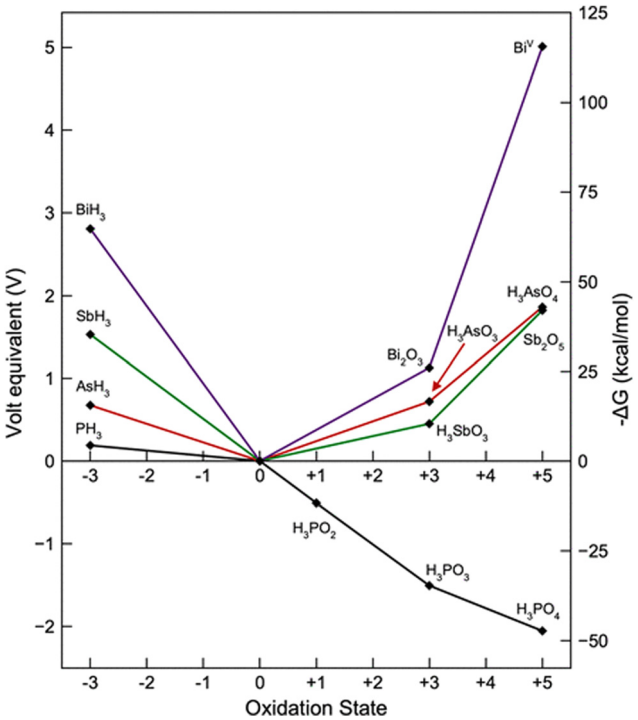

Fig. 2 Frost diagram for Pn elements under acidic aqueous conditions. Image reproduced with permission from ref. 14.

different stability of bP in comparison to the other Pn analogues. This results in the well-known oxophilic behaviour of phosphorus, which triggers the low environmental stability of bP.[15] In the case of the other pnictogens, the oxidation tendency decreases from Bi to As, for both oxidation states: +3 or +5.

Furthermore, in the 2D limit, due to the presence of the extra nonbonding electron pair in every single atom, the surface of these layered materials can be considered as a massive delocalized 5 electron cloud, endowing the materials with a characteristic chemical feature. For instance, in the case of bP, this behaviour could play the role of a soft nucleophile in certain types of chemical reactions.[11] This provides a characteristic chemical reactivity to 2D-Pn that needs to be explored. Additionally, as soon as the principal quantum number increases, the radial distribution function of the p orbitals extends, thus the interlayer interaction becomes stronger, making their exfoliation complicated. This effect, which can be rationalised as a function of the out-of-plane:in-plane ratio, hinders the obtaining of few-layer flakes with large areas by top-down techniques, as generally demonstrated by Backes *et al*,[6] and even proved by our group in the case of μME Sb flakes.[16]

Different is the case when the layered materials also present electrostatic interactions, such as layered double hydroxides. Here, the electrostatic energy is summed to the typical van der Waals interlayer interactions observed in 2D materials. Therefore, the delamination process required the stabilisation of charged layers as well as the solvation of intercalated anions.[17–20] Along this article we will introduce the important double role played by the solvent in Pn's exfoliation process: physical (colloidal stability) and chemical (passivation, protective layer) stabilisation of the colloidal suspension.

With respect to the electronic properties of 2D-Pn, one of the most interesting points is their acute band gap layer-dependency. Indeed, bulk bP was reported to have a band gap of ~0.31 eV, that increases with the reduction of the layer number, reaching ~2 eV for monolayer bP.[2] This increment in the band gap has been also calculated by DFT and reported for the other Pn, showing from metallic (trilayer As, bilayer Sb, and trilayer Bi) to insulator or semiconductor behaviour in the case of the monolayer (2.49, 2.28, and 0.32 eV for As, Sb and Bi, respectively).[9,21,22]

Regarding preparation methods, the more established approaches for other 2D systems such as graphene or TMDs have been successfully used for the production of bP and antimonene.[23–25] Interestingly, the isolation of 2D bP has undergone a similar historical development as that of graphene. Indeed, despite its discovery dating to 1914,[3] and its crystallographic description to 1935,[4] its introduction in the realm of 2D material's family took almost 100 years. Indeed, the first isolation of single-layer bP (phosphorene) only occurred in 2014.[2] Considering graphene as a reference example, bP can be produced by using common top-down techniques, including liquid phase exfoliation (LPE),[24,26] electrochemical exfoliation,[27–29] and bottom-up methods, such as CVD,[30] pulsed laser deposition (PLD),[31] and even solvothermal synthesis.[32] Similarly, also for As, Sb and Bi bottom-up and top-down approaches have been developed, but in this case with disparate success.[23,33–36] Indeed, the exfoliation of Pn using top-down routes like LPE is less efficient compared to other 2D materials. This is due to the external energy (*e.g.* sonication) required to overcome the strong interlayer interactions resulting in crystals breaking and downsizing (typically <300 nm in lateral dimensions), leading to non-homogeneous sheet morphologies.[37] As the interlayer interactions increase along the group, highly anisotropic 2D-Bi flakes will be extremely difficult to achieve by LPE or related top-down approximations. Hence, the most promising route for the synthesis of heavy Pn lies in the use of bottom-up approaches.[38,39] In fact, large-scale production of high-quality layered heavy Pn has been demonstrated by colloidal synthesis,[40] a strategy that relies on chemists' background.

In this feature article, we will present the research contribution carried out by our group and close collaborators on the emergent field of 2D-Pn nanomaterials emphasising the chemical approach as a promising alternative for the synthesis and investigation of their properties. To this aim, we are proposing and will employ along the manuscript a careful distinction of Pn's production. Specifically, the term "synthesis" will be only employed for bottom-up approaches, referring to those methods involving molecular precursors and chemical reactions.

The *fil rouge* across our work encompasses several aspects of fundamental research on Pn materials that can be resumed as follows: (i) production and chemical control, (ii) development of fundamental knowledge on the characterization, and (iii) research on the properties and applications of 2D-Pn. This article

Open Access Article. Published on 21 April 2023. Downloaded on 5/10/2026 2:30:36 PM.
This article is licensed under a Creative Commons Attribution-NonCommercial 3.0 Unported Licence.

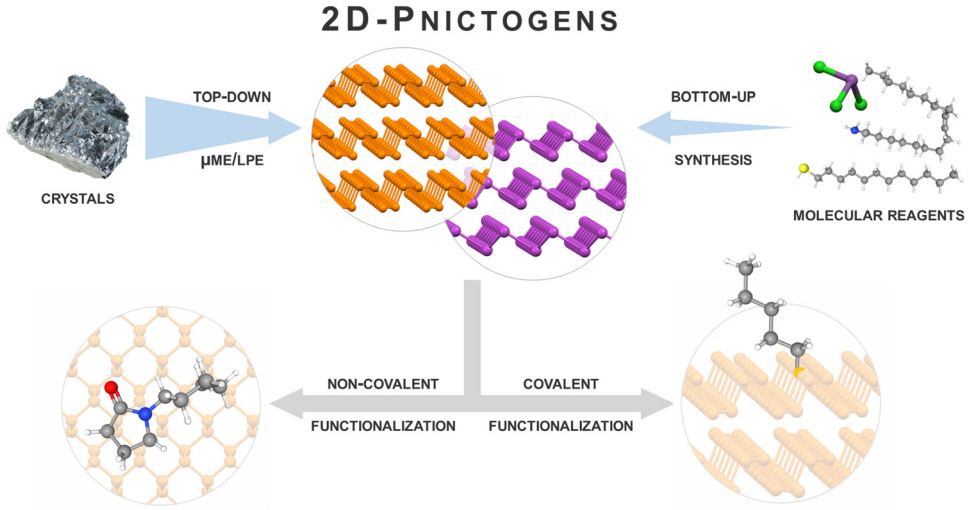

Scheme 1 Main concepts discussed along this work. The production of 2D-Pn can be achieved using physical top-down approaches such as micromechanical and liquid-phase exfoliation of macroscopic crystals. In addition, they can also be synthesized by chemical bottom-up approaches, using molecular precursors, as occurs in the case of the colloidal route. Furthermore, the stabilisation and modification of the 2D-Pn properties can be performed by both non-covalent (employing solvent or tailor-made molecules) and covalent functionalization through the generation of new Pn–X chemical bonds (*e.g.*: P–C).

will guide the reader through 2D-Pn development, highlighting our contribution to its research and presenting our vision toward the future of these materials, discussing the key role that chemists should play in this exciting research field (Scheme 1).

2. Controlled production and environmental stability

2.1. Pnictogens production methods – top-down approaches

The first reports highlighting bP are from March 2014, where a p-type field-effect transistor based on few-layer bP was developed. The bP crystals were firstly produced by transforming red phosphorus into bP under high pressure and high temperature, while micrometre-scale flakes owing thickness higher than 2 nm were obtained by peeling the aforementioned crystals through Scotch tape-based mechanical exfoliation method.[2] Fifteen days later, the monolayer limit (0.85 nm) was reported, yielding the so-called phosphorene, also by mechanical exfoliation,[41] exhibiting a well-defined thickness-dependence behaviour on photoluminescence and Raman signals. Both works pointed out the high sensitivity of bP to environmental conditions in comparison to other 2D materials. Shortly after the liquid-phase exfoliation of bP employing NMP was carried out.[24] This production method – further applied also to heavy pnictogens – consists of the delamination of millimetric-sized crystals of the element by application of external energy. Commonly, the crystals are ground to reduce their size, dispersed in appropriate solvents, and subjected to sonication or shearing forces, causing the layers separation as well as sheets breaking. After centrifugation, a stable suspension can be recovered, giving nanomaterials of different size, thickness, and oxidation degrees, depending on sonication time, centrifugation speed, or solvent conditions (Fig. 3A).[6,37] In 2015, Coleman and co-workers demonstrated the advantage of using *N*-cyclohexyl-2-pyrrolidone (CHP) obtaining highly crystalline flakes (Fig. 3B–E).[15] Noteworthy, these dispersions typically exhibit FL-bP flakes of *ca.* 10 nm in thickness and <500 nm in lateral dimensions (Fig. 3F). Moreover, the employment of this solvent was fundamental to improve bP stability under atmospheric conditions, as will be discussed further in this text.

On the same pathway undertaken with bP, our group also contributed to the fundamental development of Sb-based 2D materials. Only a few months later after the first isolation of μME Sb monolayer by Zamora's group,[43] we demonstrated the feasibility of the LPE approach for the 2D-Sb production. By applying tip sonication in i-propanol/water (4 : 1) mixture of grounded Sb crystals we were able to obtain few-layer Sb dispersions. Interestingly, in both cases, the material resulted to be stable for months under ambient conditions.[42]

Applying the knowledge developed for bP, we explored the correlation between thickness and number of layers by means of AFM and Raman spectroscopy. Our experimental observation showed a pronounced decrease of the Raman intensity with the number of layers, reaching silent spectra for the thinnest flakes, in contrast to other 2D materials like graphene or boron nitride. This decrease in the intensity was supported by DFT calculations, however, the complete disappearance of the Raman signal was related to the surface oxidation of the flakes as explained below.

For the preparation of unoxidized few-layers Sb, the ionic liquid (IL) 1-butyl-3-methylimidazolium tetrafluoroborate (bmim-BF4) was used on the basis of its excellent oxidation protection behaviour for FL-bP.[11] Sonication of ground Sb crystals dispersed in bmim-BF_4 was performed in an argon-filled glovebox (<0.1 ppm of H_2O and O_2) to yield brownish,

Open Access Article. Published on 21 April 2023. Downloaded on 5/10/2026 2:30:36 PM.
This article is licensed under a Creative Commons Attribution-NonCommercial 3.0 Unported Licence.

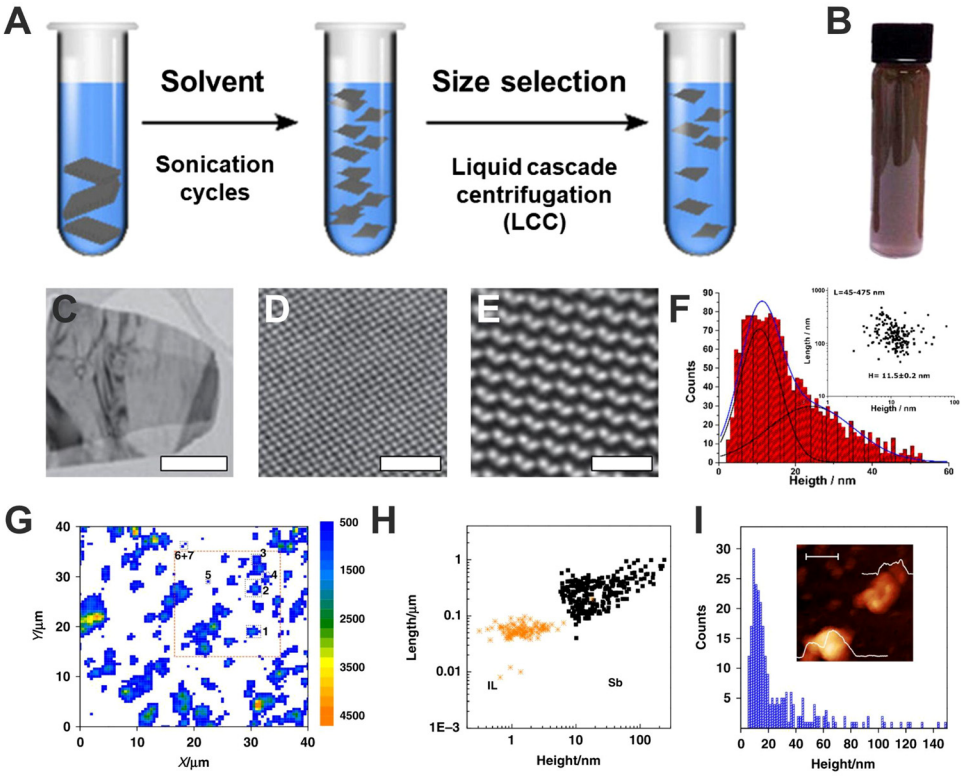

Fig. 3 General scheme of the liquid phase exfoliation and sequential size selection through liquid cascade centrifugation (A). Photograph of a dispersion of exfoliated FL-bP in CHP (B). Low-resolution transmission electron microscopy (TEM) images of FL-bP exfoliated in CHP. Scale bar: 500 nm (C). Bright-field scanning transmission TEM (STEM) image of FL-bP. Scale bar: 2 nm (D). Butterworth-filtered high-angle annular dark field (HAADF) STEM image of FL-bP (exfoliated in isopropanol) showing the intact lattice. Scale bar: 1 nm (E). Histogram of the apparent thickness of the exfoliated FL-b1P obtained from AFM. Inset: Plot of the nanosheet length as a function of the flake height considering a total amount of 170 replicates. The average thickness is $H = 11.5 \pm 0.2$ nm and lateral sizes are ranging from 45 to 475 nm (F). Sb flakes Raman A_{1g} (λ_{exc} = 532 nm) mapping, where >14 000 single point spectra over a surface area of 40 μm^2 using a step size of 0.5 µm have been recorded (G). Plot of the nanosheet length as a function of the flake height (obtained from AFM), including the data corresponding to the control experiment for the ionic liquid, IL (H). Histogram of the apparent thickness of the exfoliated FL-Sb obtained from AFM (sample size = 271). The inset shows an AFM image of a nanosheet along with its corresponding height profiles of *ca.* 4 and 18 nm, respectively. Inset, scale bar: 100 nm (I). Figure adapted with permission from ref. 15 and 42.

open-air stable suspensions of unoxidized FL-Sb nanosheets, after removing the unexfoliated particles by a two-step centrifugation process. These samples exhibited median values of 310 nm in lateral dimensions and *ca.* 32 nm in thickness and can be stored under ambient conditions over weeks with no signs of degradation (peaks related to the formation of Sb_2O_3 or Sb_2O_5). This LPE strategy, which was initially developed for bP,[44,45] has been one of the few top-down routes allowing isolation of FL-Sb without oxidation. Despite this, it has the disadvantage of generating flakes with poorly defined morphologies, incompatible with the preparation of dispositives, although very useful for other applications beyond electronics.

Following up on these works, we performed an extensive study on Sb LPE production, aimed to improve the lateral size distribution as well as the exfoliation yield. Note that due to the increment in the interlayer interactions in comparison to bP, yields were lower than 1% – a common result for 2D materials exfoliation. Thus, we carried out a systematic study on the experimental conditions, considering from the pre-treating protocols (manual grounding, dry and wet ball milling) to the solvent selection and exfoliation methodology (tip or bath sonication).[42] We demonstrated that while NMP:water mixtures enhance the final yield, 2-butanol increases the dimensional anisotropy ratio (defined as the ratio between the length and height of the nanolayers) (Fig. 3G–I). Interestingly, FL-Sb obtained from 5 : 1 NMP : water mixture exhibits a lower oxidation degree probably due to the formation of a protective layer onto Sb flakes' surface. Furthermore, when these Sb-based samples are compared in terms of hydrogen evolution reaction (HER) activity, the one obtained from 2-butanol exhibits better performance probably due to the irreversible formation of antimony oxide and the lack of a solvation protective shell.

Regarding 2D-As and Bi, their production was achieved with similar, and often the same, production methods of 2D-Sb. In example, shear force exfoliation using common kitchen blenders in aqueous media was employed to exfoliate pnictogens crystals, giving few-layer As, Sb, and Bi nanoplatelet.[23] Besides, this method induced oxidation of the exposed surface and formation of Pn-oxides during the process. The same group, in a following study, achieved the production of low-oxidised and ultra-thin As sheets (2–4 nm) by LPE using NMP as solvent,[46] as previously demonstrated for bP.[15] Hang Qi *et al.*

Open Access Article. Published on 21 April 2023. Downloaded on 5/10/2026 2:30:36 PM. This article is licensed under a Creative Commons Attribution-NonCommercial 3.0 Unported Licence.

elucidated by DFT calculation the interaction effect of arsenene surface and solvents, to replace high-boiling point solvents and simplify 2D-As processing. Low-boiling point solvents such as THF, chloroform and cyclohexane were reported to have the best absorption energy/transfer energy ratio, and yielded slightly oxidised nanosheets with thickness between 33 to 49 nm.[47] In a very interesting study, Wu and coworkers reported the production of the less thermodynamically stable α-arsenene (called black-arsenene (bAs) over the most famous bP). The researchers obtained layers of several micrometers of lateral dimensions by μME, and demonstrated that 2D-bAs possess high anisotropies along AC and ZZ, directions in its conductance, carrier mobility, and thermal conductivity.[48] In the case of bismuthene, bulk Bi is harder to exfoliate because of its greater interlayer interactions. Indeed, to the best of our knowledge, bismuthene μME exfoliation has not yet been reported. Therefore, novel assisted exfoliation methods have been developed, besides common LPE.[49] In one example, a new exfoliation strategy combining water exfoliation with H_2O_2/H_2SO_4 intercalation was developed.[50] Sulfuric acid intercalation occurs by means of hydrogen peroxide gas formation, which expands Bi structure, facilitating the acid intercalation. Furthermore, the nanosheets (average lateral size 735 ± 297 nm and thickness of 6.7 ± 3.2 nm) were purified by solvent exchange with NMP.

Table 1 summarises some of the most typical bottom-up approaches for 2D-Pn production.

2.2. Controlled production of pnictogens nanomaterials

At this point of the discussion, the main limitation of top-down approaches (and mainly LPE) applied to Pn production must be highlighted. Despite the efforts reported on the materials' optimization, pre-treatment, and solvents selection, the aspect ratios are relatively small in comparison with other 2D materials such as graphene. Within the group, these differences are also more remarkable, mainly due to the increment in the interlayer interaction when descending from P to Bi. Considering that the aspect ratio of the exfoliated material is highly dependent on the in-plane:out-of-plane forces,[37] the increment in the interlayer interactions for heavy Pn will make it difficult to obtain high quality large FL Sb and Bi.

To date, one of the few examples of controllable top-down approach is represented by the achievement of phosphorene nanoribbons (PNRs).[51] Howard and co-workers, by means of a LPE approach, obtained monolayer PNRs with nanometric width (4–50 nm) and length up to 75 μm, corresponding to an aspect ratio up to 1000. The production follows a first step of bulk bP intercalation with metallic lithium (detailed description of this method will be found at paragraph 3.2 covalent functionalization, *vide infra*) followed by gentle shaking and separation by sedimentation. The authors also suggest that the breaks occur on longer P–P bonds in the zigzag direction, due to increased strain between intercalated and non-intercalated zones.[51,73] PNRs were further employed to produce hybrid solar cells, acting as an effective charge-selective interlayer by enhancing hole extraction from polycrystalline perovskite to the semiconductor, as predicted in several theoretical investigations.[74–76]

As chemists, we consider that the solution for producing large anisotropic 2D layers of heavy pnictogens will come from bottom-up wet-chemical approaches.

Several examples of colloidal approaches controlling size and morphology are present in literature. In the case of pnictogens, generally Pn(III) salts and the common reducing agents for metallic nanoparticles synthesis (*e.g.*: $NaBH_4$, NaH, N_2H_4 oleylamine, and dodecylamine)[77,78] have been employed to obtain of As,[53,79] Sb[56,57,79] and Bi nanoentities.[62,67,79] Table 1 compiles some selected examples of these syntheses. Among these, we would like to highlight a study exemplifying the great potential of chemistry for on-demand controlling size and morphology nanomaterials. Buhro and co-workers reported the controlled synthesis of metallic β-Bi spherical nanoparticles (<25 nm), hexagonal nanoplatelet (*ca.* 100 nm) and nanoribbons (<50 nm width and >2 μm length) from a colloidal point of view, exclusively.[72] We envision that this pioneering work represents a starting point for the synthesis of larger and thinner Pn-based 2D nanomaterials.

Indeed, the first wet-chemistry colloidal synthesis for 2D-Sb dates from 2019. Large hexagonal crystals of Sb exhibiting lateral sizes up to 1.5 μm and thicknesses ranging from 5 to 30 nm were obtained by controlling the anisotropic growth in a colloidal mixture of organic solvents.[39] More in detail, the synthesis of Sb-based hexagonal crystals consists of a two-step hot-injection approach. Firstly, the precursor is prepared by dissolving antimony chloride into a dodecanethiol (DDT) and 1-octadecene (ODE) mixture at 110 °C for 2 h under vacuum conditions, and then heat up to 150 °C to trigger the reaction. Afterward, the precursor is injected into a oleylamine (OA) and ODE mixture at 300 °C, giving rise to the formation of the hexagonal crystals.[39] Less than a year later, in 2020, the same authors reported a modified protocol that permits the synthesis of both Sb and Bi well-defined crystals.[38] From these two pioneering works, our group set about optimizing the synthetic parameters to produce high-quality few-layer Sb hexagons (Fig. 4A).[40] The accurate selection of the initial conditions allow the tuning of size from 200–300 nm to 2–3 μm, and the systematic analysis of the synthetic conditions revealed the tremendous influence of the solvent used on their final surface oxidation, being chloroform the most appropriate one for keeping unoxidized surfaces (Fig. 4B–K). Furthermore, by designing a continuous-flow synthesis reactor we achieved the production of high-quality few-layer Sb hexagons in large quantities (*ca.* 1 mg h^{-1} (Fig. 4L)). Additionally, we have tested the electronic properties of our colloidally obtained Sb crystals, which indeed compete favourably with those produced by micromechanical exfoliation. These results highlight the role of colloidal-based synthetic methods to produce a large number of high-quality Sb crystals with the desired electronic properties. Later on, Torres *et at.*[68] presented another synthetic protocol for the isolation of hexagonal Bi micro-scale crystals under milder conditions than those reported for Sb. These Bi-based particles exhibit surface oxidation and present excellent

Open Access Article. Published on 21 April 2023. Downloaded on 5/10/2026 2:30:36 PM.
This article is licensed under a Creative Commons Attribution-NonCommercial 3.0 Unported Licence.

Table 1 Morphological properties of selected nanoparticles and 2D-pnictogens obtained by top-down and bottom-up approaches

Morphology	Size; thickness (nm)	Preparation methods	Ref.
P			
Nanosheet	∼1.5 micrometers (0.85 nm)	μME	41
Nanosheet	∼100–350 nm (3.5–5 nm)	LPE	24
Nanosheet	∼100 nm–3 μm (0.5–0.7 nm)	LPE	15
Nanosheet	100–200 nm (1–15 nm)	Solvothermal	32
Nanoribbons	75–1000 μm (4–50 nm)	Intercalation of lithium ions in ammonia based solvent	51
As			
Spherical nanoparticles	∼67 nm	Colloidal	52
Nanoparticles	30–164 nm	Colloidal	53
Nanosheets	100–900 nm	Liquid-phase shear exfoliation	23
Nanosheets	Several micrometers (2.9–3.5 nm)	μME	48
Nanosheets (NS) Nanodots (ND)	NS: Several micrometers (3 nm) ND: 100–350 nm	LPE	54
Nanosheets	Several nm (5–12 nm)	LPE	46
Nanosheets	100–1050 nm (33–49 nm)	LPE	47
Sb			
Nanoflakes	20–40 nm	Colloidal (microwave-assisted reduction using zinc powder)	55
Nanoparticles	∼ 2.8–6.6 nm	Colloidal (reduction with NaH)	56
Irregular and spherical nanoparticles	∼24.2 nm (13.1–23.5 nm) Diameter of ∼4.6 nm	Colloidal (hot-injection procedure)	57
Nanosheets	Several micrometers (below than 100 nm)	μME	43
Nanorods	200–300 nm (50–80 nm)	Colloidal (reduction with oleylamine)	58
Nanosheets	Few micrometers (less than 20 nm)	LPE (sonication in a mixture of 4 : 1 isopropanol/water	25
Quantum dots	∼2.8 nm	LPE (ultrasound probe sonication)	59
Nanosheets	40–300 nm (2–10 nm)	LPE (wet-ball milling in 2-butanol and liquid exfoliation using sonication tip in 4 : 1 NMP/H2O)	42
Spherical nanoparticles	34–42 nm	Colloidal (reduction using NaBH4)	60
Quasi-hexagonal nanosheets	0.5–1 μm (∼46 nm)	Colloidal (hot-injection method using alkyl phosphonic acids)	38
Nanosheets	∼3 μm (less 2 nm)	Pressurized alloying exfoliation	61
Hexagonal nanosheets	0.5–1.5 μm (5–30 nm)	Colloidal (hot-injection method)	39
Hexagonal nanosheets	∼6 μm (4–20 nm)	Colloidal (continuous-flow procedure)	40
Bi			
Spherical nanoparticles	11–22 nm	Colloidal (hot-injection procedure)	62
Nanowires and nanoflowers nanoparticles	∼20 nm	Colloidal (solvothermal method)	63
Nanoparticles	40–80 nm	Colloidal (using hexadecyl amine as reducing agent)	64
Spherical nanoparticles	∼4 nm	Colloidal (with ocatadecylene/oleic acid)	65
Nanoparticles (NP) Nanobelts (NB)	NP: 10–50 nm NB: several μm (10–100 nm)	Colloidal (reduction reaction using $NaH_2PO_2{\cdot}H_2O$)	66
Spherical (S), cubes (C) and triangular (T), and nanobelts (NB) nanoparticles	S: 20–200 nm of diameter C: 60–80 nm of edge length T: 200–500 nm NB: ∼80 μm (0.6 μm)	Colloidal (polyol process)	67
Quasi-hexagonal nanosheets	100–500 nm	Colloidal (hot-injection method using alkyl phosphonic acids)	38
Hexagonal nanosheets	0.5–7.5 μm (below 20 nm)	Colloidal (hot-injection method)	68
Nanosheets	∼20 nm (2 nm)	Ionic liquid assisted exfoliation	69
Nanosheets	∼0.8 μm (∼4 nm)	Sonochemical exfoliation	49
Nanosheets	735 ± 297 (6.7 ± 3.2 nm)	Acid intercalated exfoliation	50
Nanosheets	50–200 nm (∼9 nm)	Electrochemical exfoliation	70
Irregular shape nanoparticles (I), quasi-hexagonal nanosheets (H) and spherical nanoparticles (S)	I: 80–120 nm H: 700–900 nm (7–12 nm) S: 10–19.4 nm	Colloidal (solvothermal procedure using hydrazine)	71
Dots (D), nanoplates (Np), nanorods (Nr)	D: 30–45 nm Np: ∼50 nm to ∼100 nm Nr: ∼20 nm × ∼80 nm	Colloidal	72

mechanical and electrical properties that can be employed in NADH sensors, where Bi material acts as an electrocatalytic platform owing to a high charge transfer during donor–acceptor processes.

As a summary of this part, we would like to confront the efficacy of Pn production methodologies. Table 1 summarises the main morphological characteristics of Pn produced by top-down and bottom-up approaches, highlighting the importance

Open Access Article. Published on 21 April 2023. Downloaded on 5/10/2026 2:30:36 PM.
This article is licensed under a Creative Commons Attribution-NonCommercial 3.0 Unported Licence.

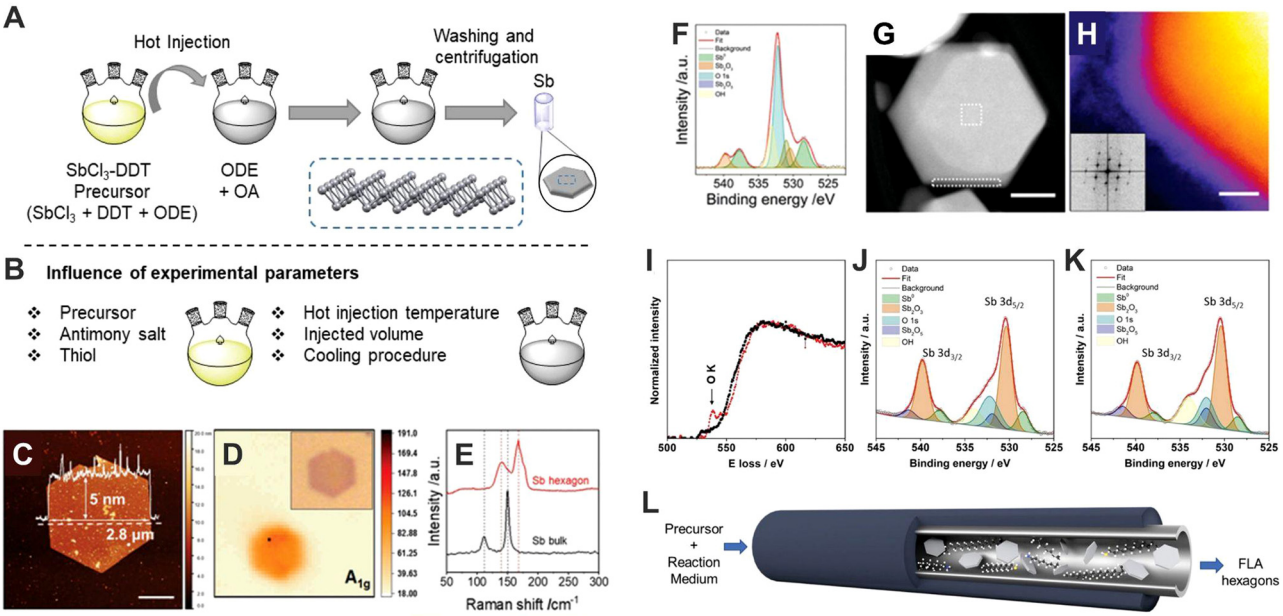

Fig. 4 Schematic representation of the synthetic procedure (A). Summary of the experimental parameters influencing the reaction (B). AFM profile of hexagonal Sb nanosheets with overlaid thickness profile (5 nm height over 2.8 µm diameter). Scale bar of 1 µm (C). Raman mapping of A_{1g} (150 cm^{-1}) intensity with optical micrograph given as inset (D). Raman signal comparison of bulk antimony and Sb hexagonal nanosheet (E). Typical XPS line spectra of Sb 3d 5/2 and 3/2 region for Sb hexagonal nanosheets (under environmental conditions) showing contributions from both metallic and oxidised Sb components. Individual contributions from the fitting are highlighted (F). HAADF STEM image of an individual nanosheet (G). Coloured high-resolution STEM-HAADF image to emphasise the amorphous edge surrounding the particles. Inset shows the FFT demonstrating the crystallinity of the material. Scale bar of 5 nm (H). EEL spectrums of FLA hexagon dispersed in chloroform (black) and dispersed in IPA (red) (I). Typical XPS line spectra of FLA hexagons synthesised by continuous flow procedure dispersed in chloroform (J). Typical XPS line spectra of FLA hexagons synthesised by continuous procedure dispersed in IPA (K). Schematic representation of continuous flow synthesis (L). Figures adapted with permission from ref. 40.

of colloidal synthesis as the most efficient and reproducible approach for the production of heavier 2D-Pn.

2.3. Black phosphorus environmental stability

Research on bP has been marked since the first studies published by its low stability under ambient conditions, regardless of the production method, affecting the material by fast decomposition due to oxidation.[80] At the very beginning, several researchers attributed the droplet formation on bP surface to the water condensation due to air moisture presence.[80–82] Nonetheless, some works demonstrated that the use of deaerated water or solvents diminished the material decomposition. Indeed, this environmental degradation was due to the chemisorption of O_2 onto bP surface that induces its dissociation triggering the oxidation of the pristine material by the formation of P_xO_y species. Then, the presence of water leads to the formation of phosphoric acid and as a consequence the solubilization of these formed species promotes degradation.

In this framework, in collaboration with Prof. Coleman's group, we investigated whether it was possible to use new solvents capable of promoting exfoliation and at the same time preventing bP oxidation.[15] For instance, CHP was found to be a good candidate to exfoliate bP under ambient conditions, allowing the preparation of suspensions of stable bP flakes for days (Fig. 5), much longer than the first observation of *ca.* 1 hour of stability for µME flakes.[81] Motivated by this result, sodium cholate, was also employed as surfactant due to its well-known role as an exfoliating agent in water-based mixture.[6,83] Nevertheless, besides bP exfoliation can be carried out successfully, the reported stability is much lower in comparison to that obtained with CHP. Thus, it was hypothesised that the stabilisation relies on the ability of CHP to form a solvation shell on top of the bP surface. Keeping this in mind, the solvent/surfactant selection must cover two important aspects: (i) be able to exfoliate and prevent reaggregation of the sheets, as it was usually thought for 2D materials in general; (ii) protect the surface from oxygen interactions by forming a compact protective layer (solvation layer), avoiding further degradations. Hence, this fact limits the number of solvents or surfactants that can be employed for the successful preparation of bP suspensions.

As the rapid oxidation of bP is one of the major limitations for the characterization of this material, with the group of Prof. Hirsch we developed a methodology based on statistical Raman spectroscopy (SRS) to monitor the degradation of few-layer bP.[45] Employing the influence of bP anisotropy on A_{1g}/A_{2g} Raman band (indicative of the oxidation state),[15,84] we compared SRS with AFM measurements. Data were collected every 24 h, showing clear evolution of Raman bands ratio along time, more pronounced after 72 hours. The development of A_{1g}/A_{2g} ratio distribution as a function of time allowed to follow the environmental degradation of bP, showing an exponential

Open Access Article. Published on 21 April 2023. Downloaded on 5/10/2026 2:30:36 PM.
This article is licensed under a Creative Commons Attribution-NonCommercial 3.0 Unported Licence.

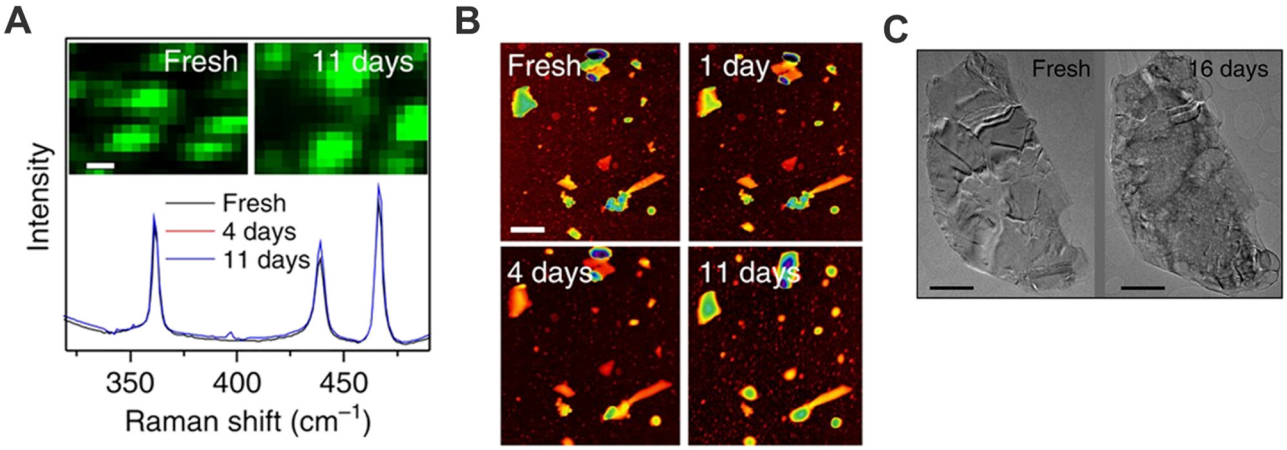

Fig. 5 bP flakes obtained by LPE employing CHP as solvent: mean Raman spectra (λ_{exc} = 633 nm) summed over the region of an as-prepared sample as a function of exposure time. Spectra are normalised to the silicon peak at 521 cm^{-1}. Inset: Raman A_{1g} intensity map of the sample region (A). Sequence of AFM images of the same sample region of an as-prepared sample, and after 1, 4 and 11 days of exposure to ambient conditions, respectively (scale bar, 600 nm) (B). TEM images of the same flake deposited from a freshly prepared dispersion and after 16 days (C). Figure adapted with permission from ref. 15.

decay trend of the Raman band ratio intensity. Additionally, the same study also demonstrated that visible light can promote a faster degradation process. In addition, we were able to demonstrate the important role played by both flake thickness and lateral dimensions in bP oxidation kinetics, an important aspect to consider when comparing results.

Once understood how to control the bP degradation, this oxidative behaviour was employed as a soft chemical exfoliating tool to reach the monolayer bP. Indeed, by exposing micromechanical pre-exfoliated bP under ambient conditions, followed by washing with deoxygenated water, the bP thickness can be reduced layer-by-layer following iterative cycles. It is worth mentioning the quality of the obtained flakes is good enough to prepare FET showing competitive mobility values.[85] Furthermore, to achieve high-quality unoxidized few-layer bP by LPE it is recommended to work under inert conditions, and preferably using NMP as a solvent and an Ar-filled glove-box ($<$0.1 ppm O_2 and $<$0.1 ppm H_2O), avoiding oxidation and decomposition of the catalyst.[15] Afterwards, to avoid the presence of NMP–which precludes a proper characterization of the flakes by AFM, among other fundamental techniques–the FL-bP can be transferred to THF by sequential ultracentrifugation and re-dispersion using increasing centrifugation speeds, leading to stable dispersions with $<$0.01 wt% of NMP, and absence of oxidation, evaluated by the $A_{1g}/A_{2g} > 0.4$ intensity ratio statistics (average 0.79).[86]

2.4. Antimonene environmental stability

In general, one of the issues that has generated the most controversy in the preparation of antimonene has been deciphering whether the environmental stability of the material is intrinsic or due to a passivation effect as a consequence of superficial oxidation. The first indications pointing to this possibility date back to 2017 when we published a paper on the functionalization of antimonene (prepared both by μME and LPE),[87] but it was not until 2020, when we published the first systematic experimental and theoretical works investigating the formation of antimony oxide species during LPE production, unveiling the important role of oxidised species in 2D-Sb stabilisation and electronic properties.[16,88,89] Specifically, the exfoliation of Sb in water : i-propanol mixture was carried out, and the obtained materials were characterised at different times to follow the time evolution of the Sb oxidation. XPS analysis revealed an increasing amount of oxygen during the LPE process, exhibiting a combination of absorbed oxygen and antimony oxide. The spectra deconvolution allowed us to discern antimony oxidation states, starting with Sb_2O_3 formation after only 5 minutes sonication and followed by Sb_2O_5 after 20 minutes. The last aliquot after 40 minutes showed the saturation of oxide species, with the predominance of adsorbed oxygen and hydroxides formation. The samples prepared at different times were further annealed in ultra-high vacuum (UHV) at 210 °C, to remove impurities due to solvents and absorbed oxygen. The annealing process exhibited a significant increase of Sb^0 content, together with the absence of Sb_2O_5. Ultraviolet photoelectron spectroscopy (UPS) was carried out on the annealed and non-annealed samples, to obtain insight into the valence levels. After annealing, the valence band of the three samples showed a peak at ~1 eV from the Fermi level and an increase in the intensity near 0.5 eV, resulting in a semiconducting behaviour with a bandgap of approximately 1 eV. To gain further information about this oxidised layer, DFT calculations on Sb_xO_y species were performed, developing a model for antimony oxide on which the oxygen atoms are incorporated in the sheets (type II in Fig. 6A).

We hypothesise that the formation of a superficial antimony oxide layer, different to what was demonstrated for bP,[85] can protect the material from further oxidation. Moreover, these layers are semiconducting, with direct and indirect band gaps between 2.0 and 4.9 eV. Based on these calculations and the

 This journal is © The Royal Society of Chemistry 2023

Open Access Article. Published on 21 April 2023. Downloaded on 5/10/2026 2:30:36 PM.
This article is licensed under a Creative Commons Attribution-NonCommercial 3.0 Unported Licence.

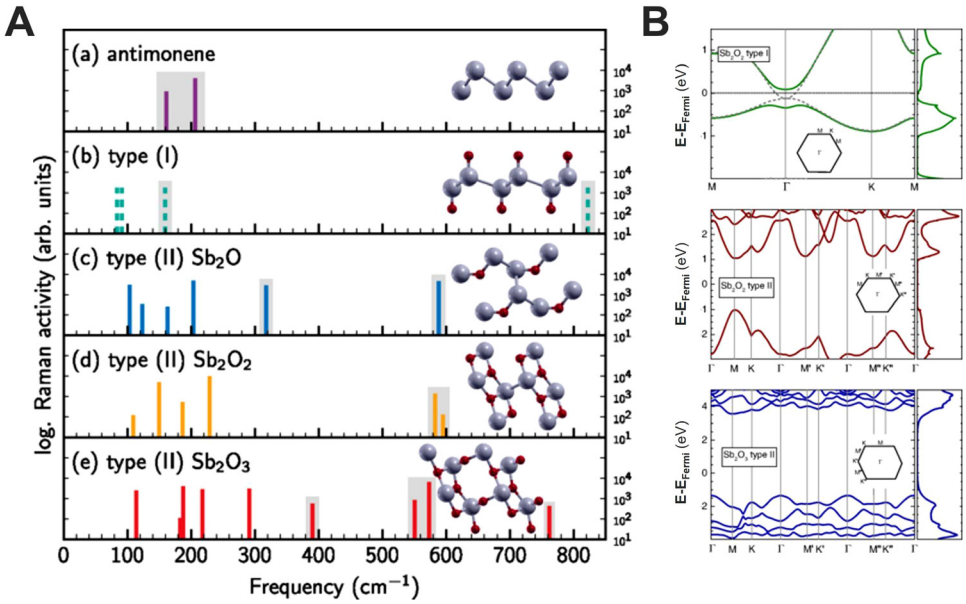

Fig. 6 Calculated frequencies of Raman-active vibrational modes in antimonene (a), and different antimony oxides (b–e). Except for (b), the height of the bars indicates the calculated Raman activity in logarithmic scale (A). Electronic band structures and density of states were calculated using the hybrid functional HSE12 and the inclusion of spin–orbit interactions (SOI) for two different Sb_2O_2 structures and Sb_2O_3 monolayers. Gray dashed lines are the results without SOI and are almost congruent with the bands with SOI. The zero of energy is set to the Fermi energy (B). Figure adapted with permission from ref. 88.

experimental data, we believe that the formation of layered heterostructures of semimetallic FL-Sb coated by semiconducting 2D Sb_2O_3 layers can naturally be formed (Fig. 6B).[89] In addition, the frequencies of Raman-active vibrational modes of these species were calculated, providing clear fingerprints for the identification of antimonene oxides, and showing good agreement with our experimental findings. Moreover, these studies rule out the formation of antimonene oxides consisting of the formation of Sb═O bonds [type (I)], leading in turn, to oxygen atoms incorporated into the antimonene sheet [type (II)].[89]

Along this front, we studied the photothermal oxidation in antimonene. For this we used μME Sb-based nanosheets using viscoelastic adhesive film with high sticking coefficient, confronting the tape with a second piece of adhesive film while pressing and rapidly releasing from each other in an iterative process. This exfoliated material consisted of polygonal shapes with smooth surfaces and sharp edges, showing atomic terraces of *ca.* 1 nm and thickness in the range of 15 nm. Interestingly, a linear temperature dependence of the position of the Raman modes was observed, explained by the phenomenon of anharmonic lattice vibrations mediated by phonon–phonon interactions (Fig. 7A and B). We extracted the first-order temperature coefficients for the A_{1g} and E_g modes $\chi = -0.027$ and $\chi = -0.025$ cm^{-1} K^{-1} (Fig. 7C), respectively, and estimated a thermal conductivity value of *ca.* $K_{Sb} = 90$ W m^{-1} K^{-1}. For that, we fixed the laser power to 0.88 mW, in order to avoid laser-induced oxidation. A phenomenon that starts at 593 K leads to the appearance of the Raman signals associated with the surface formation of the α-phase of antimony oxide (α-Sb_2O_3). This observation falls in line with the reported low lattice thermal conductivity of antimonene and suggests a high figure of merit for application in thermoelectric devices, being described by a combination of laser power- and wavelength-dependent studies with a numerical heat transfer model (Fig. 7D–F). Moreover, by adjusting the laser power and using a spatially resolved Raman mapping, it is possible to control the surface photo-oxidation of antimonene (Fig. 7G–H) paving the way for the experimental realisation of arbitrary heterostructures of Sb_2O_3/antimonene. These exotic structures exhibit great potential in optoelectronics, promoting the cytotoxicity of cancer cells and even improving the catalytic activity towards different reactions.[16]

3. Pnictogens functionalization

As developed for other materials, it is expected that the Pn properties can be tuned by rational chemical functionalization of their surfaces. Covalent and non-covalent functionalization were largely investigated for graphene and other 2D materials, proving the capability of chemistry to improve their processing, introduce new functionalities,[90] tuning their band gap[91] or improving biocompatibility,[92] to mention a few.[93,94] Besides both kinds of functionalizations can enhance stability and modulate electronic properties, the main difference between them lies in the new chemical bonds created between superficial pnictogen' atoms and the functionalizing molecules, altering the structural integrity.[95,96] For that, these two approaches will be discussed separately.

Open Access Article. Published on 21 April 2023. Downloaded on 5/10/2026 2:30:36 PM.
This article is licensed under a Creative Commons Attribution-NonCommercial 3.0 Unported Licence.

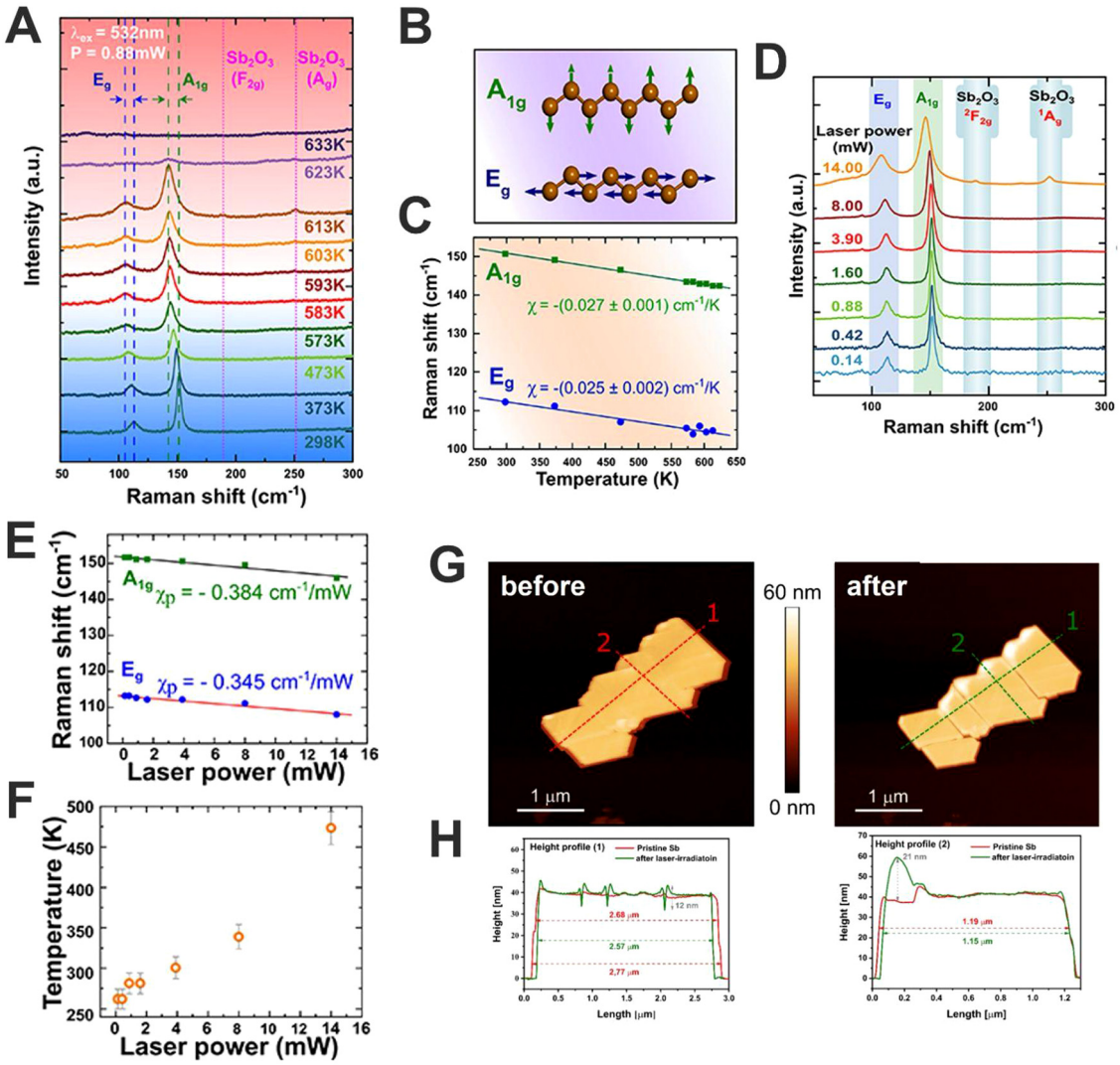

Fig. 7 Raman spectra of Sb nanosheets (Sb-NS) measured as a function of temperature from 298 to 633 K (A). Schematic diagrams of Raman active modes. Green and blue arrows indicate the direction of the atomic vibrations (B). Temperature dependence of the Raman peak positions for the A_{1g} (green squares) and E_g (blue circles) modes (C). Raman spectra of Sn-NS measured as a function of excitation laser power (λ_{exc} = 532 nm) from 0.14 to 14 mW (D). Power coefficients, χ_p, for both two modes (green squares and blue circles for A_{1g} and E_g, respectively) are extracted from the slope of the linear fits (solid lines) (E). Temperature of the probed Sb-NS as a function of laser power, was estimated using both calculated power and temperature coefficients (F). AFM image of an isolated Sb-NS before and after spatially-resolved mild oxidation using 532 nm laser at 3.9 mW for 10 s (G), height profile along the dashed red and green lines before and after laser-induced oxidation, respectively (H). Figure adapted with permission from ref. 16.

3.1. Non-covalent functionalization

Whatever the selected approach, the obtaining of 2D-Pn leads to an increment of the surface area and therefore their intrinsic reactivity. For instance, when this process occurs in presence of O_2 it provokes their oxidation, affecting the electronic properties of Pn. Thus, as a first alternative to enhance the Pn's stability, we should focus on the active lone pairs of electrons located on every surface atom, which marks the soft nucleophile tendency, as in the case of bP. Taking this into account, we developed with Hirsch and co-workers the first non-covalent functionalization of FL bP by employing extended electron-poor aromatic molecules (Fig. 8A).[13] In this contribution, both 7,7,8,8-tetracyano-*p*-quinodimethane (TCNQ) and a tailor-made perylene diimide (PDIs) molecule have demonstrated to stabilise the bP flake by forming a strong and compact protective layer, also evidenced by a considerable electron transfer from bP to the TCNQ organic dopant. Additionally, we also demonstrated that the increment of planar aromatic groups in the side-chains as well as its structure promotes stronger van der Waals interactions with bP surface, affecting the packing of PDIs. Specifically, we have synthesised tailor-made PDIs having peri-amide aromatic side chains, including phenyl and naphthyl groups. The novel naphthalene-containing PDI-R3 exhibited (after the interaction with bP) significantly increased adsorption energies and vdW contributions to the adsorption energies, as predicted by our DFT calculations (Fig. 8B–H). Interestingly, by this approach harder structured packing of surface protective molecules can be achieved resulting in an

Open Access Article. Published on 21 April 2023. Downloaded on 5/10/2026 2:30:36 PM.
This article is licensed under a Creative Commons Attribution-NonCommercial 3.0 Unported Licence.

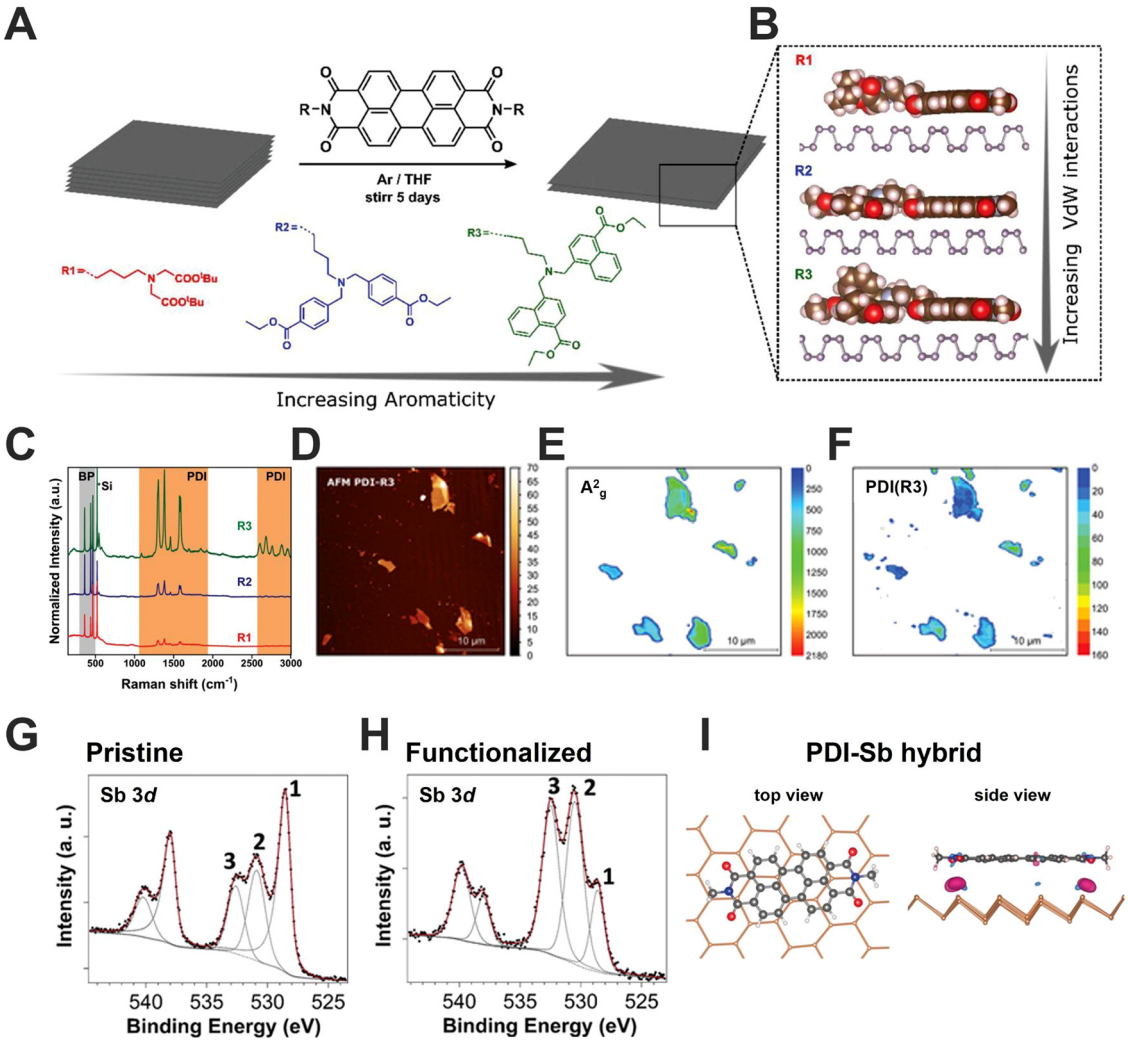

Fig. 8 Schematic representation of the general non-covalent functionalization approach of micromechanically exfoliated/grounded bP by the use of perylene diimides (PMI) with three different peripheral moieties containing aromatic groups (A). DFT-optimised structures highlight the interaction between the different PDIs and the bP surface (B). Normalised mean Raman spectra of the bP-PDI hybrids showing enhanced intensities for each of the perylene bands. The measured flakes exhibit the same heights in order to ensure the correct comparison of the intensities (C). AFM images of the μME bP flakes after hybrid formation with PDI R3 (D). Statistical Raman Microscopy of the A_{2g} bP (E) PDI representative Raman modes (1383 cm^{-1}) modes of bP-PDI R3 (F). XPS spectra of Sb 3d peak for pristine (G) and functionalized (H) Sb samples. Numbers identify the different components: 1 (Sb $3d_{5/2}$), 2 (oxidised Sb $3d_{5/2}$), and 3 (O 1s). Peaks at higher binding energy values are the Sb $3d_{3/2}$ components. The black dots are experimental points and the red line is the result of the fitting. Grey lines correspond to the different components used and the background. Top and side views of the optimised geometries of PDI core on single-layer Sb. The electron density difference between the PDI-antimonene and the isolated molecules and antimonene is also shown in the side view. Images adapted with permission from ref. 87 and 99.

increment of both environmental and thermal stability. Furthermore, beyond π extended molecules, we also showed that the oxidative mechanism can be prevented using ionic liquids, as predicted by molecular dynamics.[97] Specifically, BMIM-BF_4 (1-butyl-3-methylimidazolium tetrafluoroborate) protects similar to CHP the bP surface from the action of O_2 and water.[45] The physisorption of ionic liquids promotes the stabilisation by the formation of a physical protective layer but also by removing reactive oxygen species generated during the degradation of bP.[98]

Analogous results were demonstrated by other groups keeping in mind the typical donor–acceptor Lewis acid-base interaction.[100–102] For instance, acid cations such as Ag^+, Al^{3+} and Ga^{3+} salts have been successfully employed to increase the stability of bP under atmospheric conditions, preserving the electronic properties.[103–105]

Besides these pioneering contributions mainly based on bP, the research on non-covalent functionalization of the other Pn's members is currently under investigation. In 2017, we performed the first study on non-covalent functionalization of μME and LPE Sb flakes with PDI molecules (Fig. 8I).[87] Scanning photoelectron microscopy cooperatively with DFT calculations suggest a much stronger interaction of Sb-PDI hybrids in comparison to bP-PDI ones, resulting in a 2-fold larger

Open Access Article. Published on 21 April 2023. Downloaded on 5/10/2026 2:30:36 PM.
This article is licensed under a Creative Commons Attribution-NonCommercial 3.0 Unported Licence.

charge-transfer process, demonstrating the role of non-covalent functionalization on the electronic properties. Recently, the supramolecular functionalization of LPE Sb flakes with oligonucleotide has been carried out allowing the first steps to DNA sensor development.[106] Recently, Rao and co-workers have applied pure inorganic acid-base Lewis interactions with different moieties to enhance Sb and Bi stability.[107] Thus, non-covalent functionalization arises as an effective tool for Pn protection, keeping intact the crystalline structure and preserving the electronic properties.

3.2. Covalent functionalization

Black phosphorus functionalization through alkali metal intercalation. The covalent functionalization of Pn materials is related to the chemistry of each Pn member, not being possible an easy generalisation. Regarding bP, a first clue about its reactivity is given by its observed oxophilicity, which determines the tendency to oxidation, suggesting a strong potential reactivity of the material. The external electronic configuration of P is $3s^2\ 3p^3$, corresponding to three in-plane bonds and a lone-pair out-of-plane of the layer. When interlayer energies are minimised after exfoliation, the lone-pair is free to react, and bP can be seen as a soft nucleophile.[93] Moreover, covalent functionalization is supposed to be a surface passivation-controlled method itself, increasing the stability of the material to ambient conditions. Hersam's group, in 2016, was the first one to report the covalent functionalization of bP and prepare some FETs devices with improved ambient stability.[108] In the study, FL-bP obtained by mechanical exfoliation was deposited onto Si/SiO_2 substrate and functionalized through diazonium salts chemistry. DFT corroborates their observation, theorising the presence of thermodynamic stable phosphonium units of bP in the final structure, improving the stability of the material. Further to this study, well-known functionalization approaches were transferred to bP, *e.g.* iodonium salts and azides, among others.[109] Along this front, we carried out in 2019 the first bulk reductive functionalization of bP based on the well-established alkali metals graphite intercalation compounds (GICs). This procedure, also known as the reductive route, was previously developed to enhance graphene functionalization.[110,111] It is worth highlighting that the potential of the reductive route lies in the possibility of performing exfoliation and functionalization in a single step, resulting in higher yields and improved sample homogeneity from an overall point of view. For that we first developed a novel family of bP intercalation compounds (bPICs) with metallic Na and K, demonstrating how these species can be used to covalently functionalize bP with different organic molecules (Fig. 9A).[73,112,113]

Firstly, the bPICs formation was investigated by *in situ* XRD and Raman spectroscopy, respectively showing change from AB to AC stacking for intercalation compounds, as well as a series of novel Raman active modes, in agreement with DFT calculations.[73] Starting from that base, we demonstrated the feasibility of bP functionalization with organic molecules through the reductive route (Fig. 9B).[112] To get insight into the reactivity of bPICs, the reaction was followed *in situ* by Raman spectroscopy, evaporating in ultra-high vacuum conditions the hexyl iodide molecule in the reactor. The evolution of Raman spectra showed the arising of new active modes below 500 cm^{-1} (145, 210, 270, 320, 405 cm^{-1}) (Fig. 9C–E). Additionally, through DFT calculations the effect of the functionalization on bP was evaluated. Interestingly, and contrary to what was expected (*i.e.* the formation of phosphonium sites), the formation of P–C bonds causes the lattice opening due to the cleavage of some P–P bonds (Fig. 9F) (observed by structure relaxation and by the increasing of the length of P–P bond close to P–C bond, from 2.26 to 2.83 Å). This process was demonstrated, by using a combination of several spectroscopic techniques, to be reversible after thermal-induced retro-functionalisation.

Regardless of the covalent functionalization method used, it is necessary to quantify the degree of functionalization to have control over the properties of the material. Generally, destructive techniques such as elemental analysis (EA) or thermogravimetric analysis (TGA) are often employed, however, both require relatively high quantities of the solid material and have several limitations. To solve this situation, we developed a simple quantification method based on statistical Raman spectroscopy (SRS), correlated to quantitative magic-angle-spinning ^{31}P solid-state NMR (^{31}P-MAS NMR) as a reference technique.[114] We discovered that the evolution of C–H (2900 cm^{-1}) and P–C (645 cm^{-1}) signals in comparison to A_{2g} bP one (446 cm^{-1}), expressed as $I_{C-H}/I_{A_{2g}}$ and $I_{P-C}/I_{A_{2g}}$ ratios, directly depends on the functionalization degree (analogously to the I_D/I_G ratio employed in graphene chemistry).[110] It is important to remark here that the use of statistical Raman spectroscopy (SRS) allows for a simple and quick characterization of bP materials, not possible to achieve before without the use of more complex techniques. Indeed, we strongly recommend the use of SRS for 2D-Pn materials characterization since single-spectra analysis could induce misinterpretations. Thus, mapping large area surfaces, measuring, and analysing in an automatic way hundreds (or thousands) of spectra, will provide a better understanding of the material quality, avoiding possible bias. Despite the good results on bPICs functionalization employing alkyl iodide salts, not every reagent can be used to functionalize bP intercalation species. Aimed to improve the low yields shown by the neutral route with diazonium salts, we investigated the applications of these reagents to the reductive route. Surprisingly, after the reactions, bP was not showing the presence of functionalization. On the other hand, the material presented drastic structural evolution, with loss of crystallinity and formation of amorphous red phosphorus structures, where probably this process is promoted by intermediate radical centres on the P-lattice.[115]

3.3. As, Sb and Bi covalent functionalization

Regarding the other Pn's members, it is worth noting their covalent functionalization proceeds through the formation of bonds with semi-metallic and metallic elements. Despite the great interest in Pn materials, the reports are scarce, and only a few examples can be found in the literature about these

 This journal is © The Royal Society of Chemistry 2023

Open Access Article. Published on 21 April 2023. Downloaded on 5/10/2026 2:30:36 PM.
This article is licensed under a Creative Commons Attribution-NonCommercial 3.0 Unported Licence.

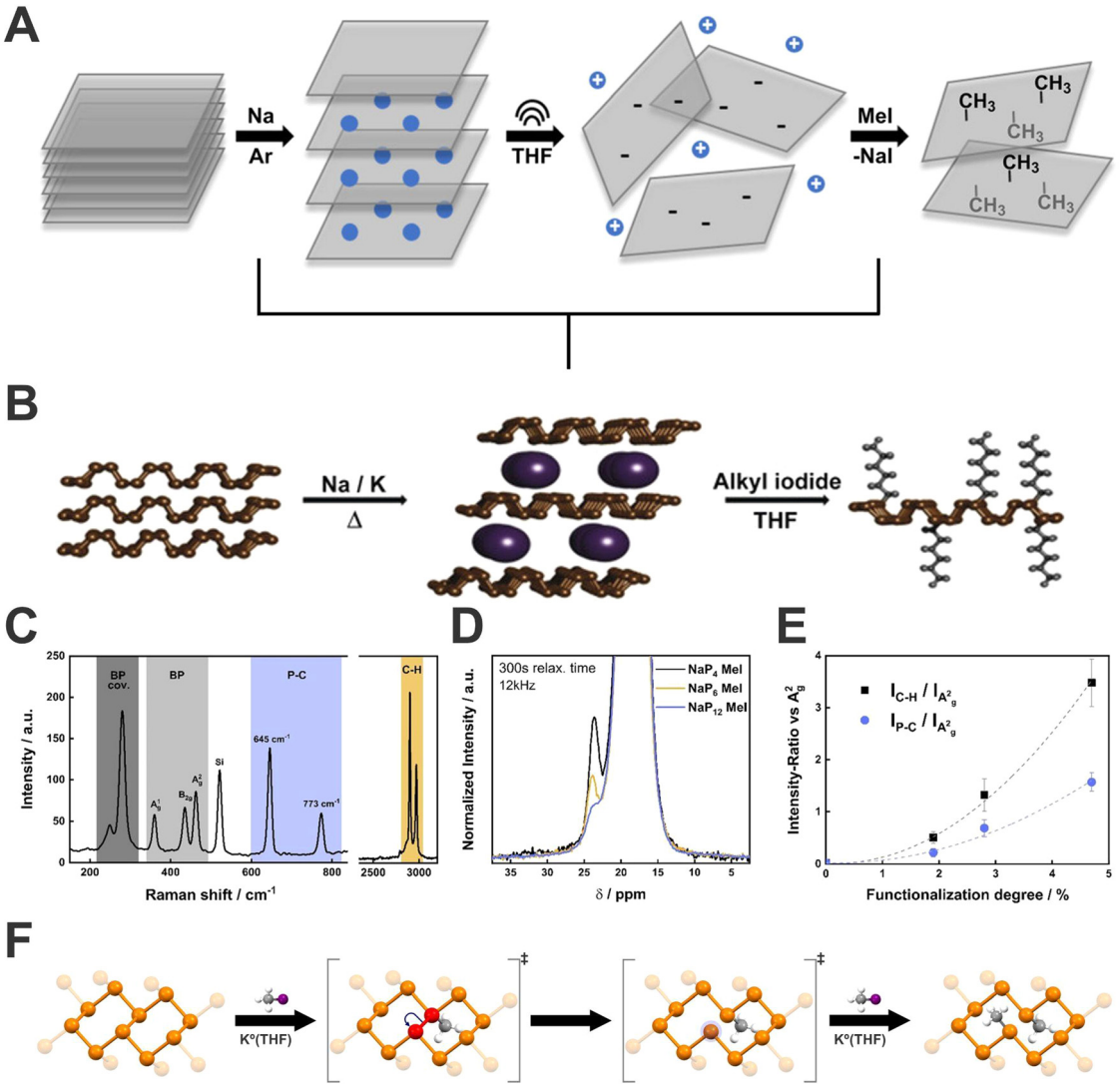

Fig. 9 Schematic representation of the sequence adopted to perform the covalent functionalization of bP (A). Generally, pristine bP is intercalated with an alkali metal in the solid state under controlled heating and afterwards, the activated bPIC is dispersed in THF and reacted with an electrophilic trapping reagent, usually a alkyl iodide (B). Mean Raman spectrum of methylated NaP_4 highlighting the different wavenumber regions (C). ^{31}P-MAS solid state NMR spectrum of methylated BP as a function of Na:P ratios (D). Correlation of the functionalization degree determined by quantitative ^{31}P-MAS solid state NMR spectroscopy to the Raman intensity ratio of the C–H and P–C vibrational mode *versus* the A_{2g} mode of bP (E). Representation of lattice opening, according to the proposed reaction mechanism, of bP upon covalent modification with methyl iodide (F). Figures adapted with permission from ref. 112 and 114.

materials. Pumera's group covalently modified 2D-As using chlorocarbene generated from organolithium and dichloromethane, yielding to the introduction of chloromethylene group. 2D-As employed was previously exfoliated by high-energy shear force milling. The researchers proposed a multi-step mechanism of functionalization, consisting first on the interaction between the 2D-As lone-pair with carbene empty orbital, followed by a rearrangement of arsenene bonds. Proofs of the occurred functionalization were obtained by HR-TEM coupled with EDS elemental mapping (energy-dispersive X-ray spectroscopy), XPS and FT-IR analysis, showing high carbon content on the materials and low oxidation degree. The functionalization caused a strong luminescence increase on the functional materials, suggesting a possible use in the optoelectronic field.[116] Direct covalent functionalization of Sb and Bi was recently reported by Rao and coworkers by means of two different approaches, one inorganic using Lewis acids,[107] and one organic employing diazonium salts as reacting species.[117] In the first example, Lewis acid of 12 and 13 group (*e.g.* $AlCl_3$, $InCl_3$, $CdCl_3$ *etc.*) reacted with 2D-Sb and Bi, yielding Lewis acid-base adducts, with the corresponding changes in the bonding environment along with lattice distortion and rehybridization of the band structure. This investigation lays its bases on the fundamental principles of Lewis acid-base theory, remarking again the importance of chemistry in the approach to pnictogens 2D materials. Interestingly, a red-shift of Raman band was observed, caused by structure distortion and charge transfer.[107] In a second article, published a few days later by the

Open Access Article. Published on 21 April 2023. Downloaded on 5/10/2026 2:30:36 PM.
This article is licensed under a Creative Commons Attribution-NonCommercial 3.0 Unported Licence.

same group, the authors demonstrate the possibility to functionalize both, 2D-Sb and Bi, with diazonium salt compounds. Exfoliated few-layers Sb and Bi were mixed in acetonitrile with pre-synthesized *p*-nitrobenzene diazonium salt (*p*-NBD). This compound exhibits a reduction potential of <0.03 V, and can be spontaneously reduced by compounds with potentials <0.06 V (Sb and Bi shows 0.212 and 0.317 V, respectively).[117] Mechanistic studies indicate the functionalization to occur by transfer of a lone pair on Sb or Bi to *p*-NBD, proposing (in the case of pnictogens) a predominantly cationic mechanism. Following a different approach, Xie and coworkers functionalized 2D-Sb exploiting the chemistry at hydroxyl groups commonly present on antimonene nanomaterials instead of direct surface modification.[118] In their work, silane-derivatives bearing epoxy groups (3-glycidoxypropyltrimethoxysilane) were employed to functionalize few-layer antimonene. Open-ring epoxidation reaction occurred at hydroxyl groups of antimonene, using aluminium(III) acetylacetonate as catalyst. The obtained Si-antimonene was then employed to produce hybrid gel glasses by silane hydrolysis and a polycondensation reaction.[118] In overall, controlled functionalization methodology of heavy pnictogens remains an open field that still presents room for a large improvement, permitting tunability of 2D-Pn properties, as well as atmospheric stability increase and introduction of new features. Moreover, the unambiguous identification of the covalent bonding remains an open challenge for the heavy pnictogens, this being a still premature topic. Indeed, the role of binding molecules on the Pn surface through Pn–X bonds with the crystal structure (*e.g.*: lattice-opening) as well as the modification of the electronic properties should be studied in greater depth to better understand the properties of these materials.

4. Pnictogens applications

As pointed out above, 2D-pnictogens exhibit a series of outstanding properties, which are ideal prerequisites for very attractive applications. Although the development of 2D-pnictogens-based applied technologies is still in its infancy, promising transistors, high-performance sensors, double-gate MOS-FETs, spintronics and optoelectronic devices, energy storage systems or applications in biomedicine have been proposed.[59,119–123] In this sense, our contribution to Pn development is not only limited to their fundamental properties and characterization techniques. Herein we are going to show some representative examples of Pn applications carried out in our group, we do not intend to be exhaustive, but merely to stimulate research in these directions by showing some interesting examples.

One of the most promising fields of application for Pn is (opto)electronics, especially in the case of bP, since it presents a layer-dependent bandgap. The development of bP-based field effect transistors (FETs) has always gone hand in hand with different strategies to preserve the devices from environmental degradation. Along this front, the noncovalent functionalization stands-out as one of the most promising ones. Indeed, a significant surface passivation can be obtained by using optimised tailor-made PDI molecules endowed with aromatic end-groups, allowing the creation of the first environmentally stable hybrid bP FETs device showing a hysteretic charge balance behaviour. The preservation of the electronic properties of bP is clearly reflected in the values of charge carrier mobilities comprised in the 130–140 $cm^2\ V^{-1}\ s^{-1}$ range corroborating that the use of these PDIs is optimal to preserve the electronic properties of bP (Fig. 10A–D).[96]

As previously shown, 2D-Pn exhibit a large chemically active surface and pronounced ability to adsorb and stabilise unsaturated organic molecules through van der Waals interactions. Owing to the control and stability against oxidation achieved on bP and Sb production we were able to investigate their potential for catalytic applications in organic chemical reactions for the first time. In 2019, we demonstrated how few-layer bP and Sb can catalyse the alkylation of soft nucleophiles with esters (Fig. 10E and F).[11] The materials, produced by LPE and stabilised with bmim-BF_4 ionic liquid, exhibited good catalytic activity for alkylation of soft nucleophiles with alkyl esters, with good performance for aromatic substrates. In addition, it was shown that the employment on Pn allows mild reactions conditions, avoiding superacid-mediated alkylation and permitting alkylation with substrate containing acid-sensitive moieties.

Moreover, in the particular case of bP, the availability of the P surface atom orbitals for external reactants together with the cooperativity of the atomic network and the possibility of reversible lattice opening (*i.e.* breaking temporarily P–P bonds) to exchange one electron,[112] would make, in principle, this 2D material a potential catalyst for radical reactions. In a detailed study with Leyva-Perez and co-workers, we demonstrated that FL-bP catalyses with extraordinary activity different radical additions to alkenes with an initial turnover frequency (TOF_0) up to two orders of magnitude higher than other metal complex catalysts at room temperature.[86] Moreover, this value was almost doubled when sodium BIPCs were employed. Comparison with other nanomaterials and their reduced forms (including graphene intercalation compound KC_8 and Fe^0 *vs.* Fe^{2-} complexes) indicates a marked increase of catalytic activity when the catalyst is negatively charged. These results represent a very promising starting point for the development of novel 2D radical catalysts based on p-block elements, and also reveal the important role played by the reactivity of these materials in their interaction with other substances, a chemical behaviour clearly different to that of graphene.

2D-Pn also demonstrated promising optical properties. Indeed, both Sb and Bi nanosheets were reported having nonlinear optical response, nonlinear refraction, and nonlinear scattering, to be potentially employed on photonic devices, laser protection devices, and all-optical Kerr switches. Example of this is represented by the previously mentioned silane-functionalized Sb nanosheets. The covalent functionalization improved their dispersibility in polymeric matrix, to which the material was covalently bonded during reaction. The produced gel glass showed strong and ultra-broad-band OL performance at 532–2150 nm.[118] 2D-Bi nanosheets dispersed in NMP, were

 This journal is © The Royal Society of Chemistry 2023

Open Access Article. Published on 21 April 2023. Downloaded on 5/10/2026 2:30:36 PM.
This article is licensed under a Creative Commons Attribution-NonCommercial 3.0 Unported Licence.

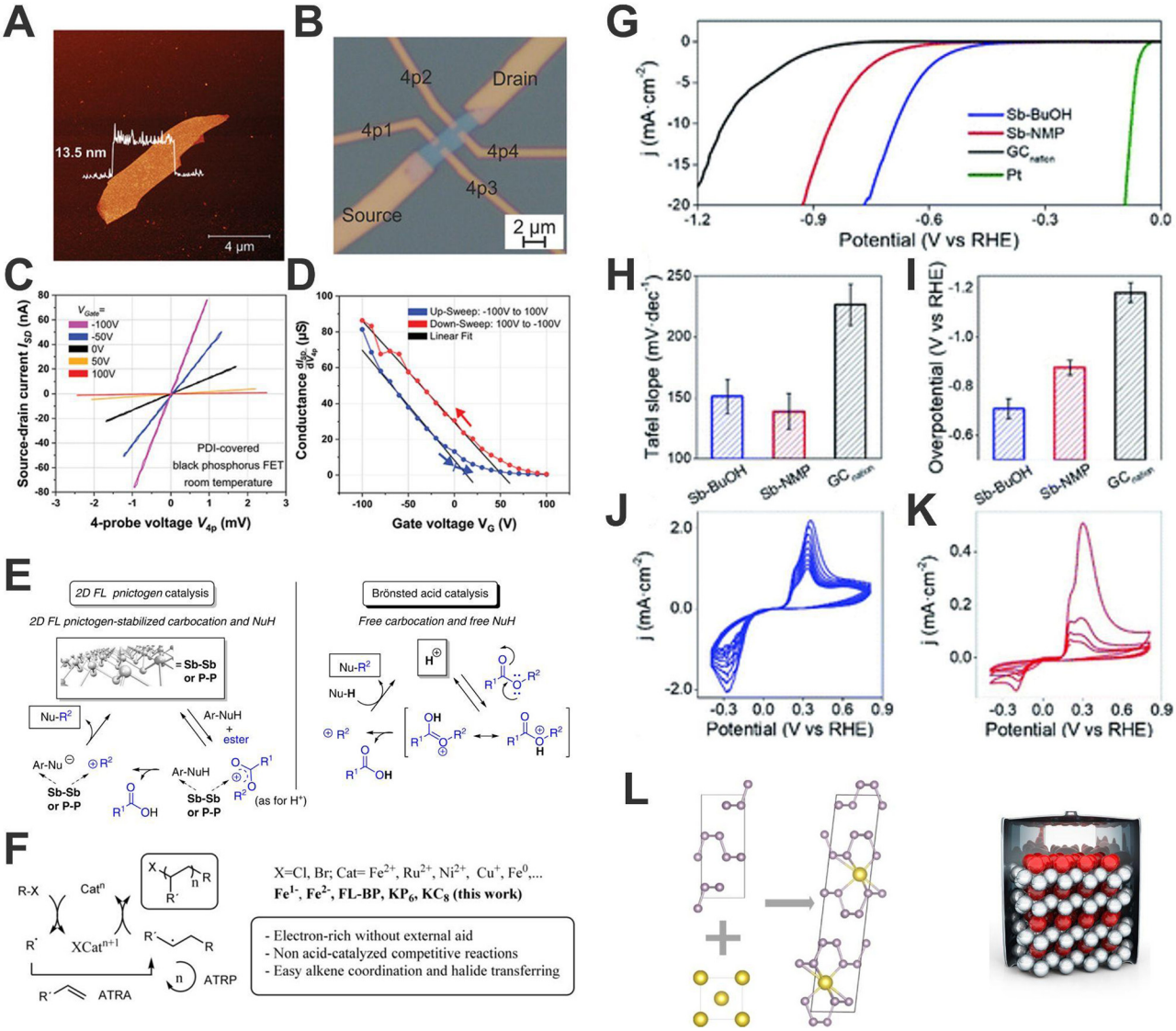

Fig. 10 Topography AFM image of the electrically investigated bP flake before processing. The height profile is shown as an overlay in the image (A). Microscope image of the processed bP field-effect transistor. The current is sent through the source and drain contacts while the 4-probe voltage is measured between the contacts 4p1 and 4p2 (B). 4-Probe current–voltage (*I*–*V*) measurements on a bP field-effect transistor for various gate voltages (each curve is averaged over 5 consecutive measurements). All *I*–*V* characteristics are perfectly linear (C). From the slopes the gate-dependent conductance is obtained and displayed in (D). The gate-voltage sweep presents a hysteresis with two branches (blue and red curves) with a seamless closure at V_G = 0 V (D). Catalytic studies by employing Pn materials. Experimental evidence and proposed mechanisms for bP, Sb, and superacid triflic acid (HOTf) catalysed-alkylation of nucleophiles with esters in ionic liquid (E). Plausible mechanism for the bP and low valence Fe-catalysed atom-transfer radical addition (ATRA) and polymerization (ATRP) reactions (F). Electrochemical characterization in terms of HER for Sb-based materials obtained through different sonication methods. LSV curves of the different Sb-based samples, Nafion modified glassy carbon and platinum blank (G). Tafel slope values (H) and overpotentials required for achieving 10 mA cm^{-2} calculated from LSV data (I). CV curves recorded after LSV measurements of Sb-BuOH (J) and Sb-NMP (K). The study of the parameter affecting the formation of the sodium/black phosphorus intercalated (bPIC) phase *via* solid-state reaction can provide fundamental details towards sodium-ion batteries based on Pn material electrodes (L). Figure adapted with permission from ref. 86, 44, 42, 99 and 113.

dropped onto a gold mirror, exhibiting a nonlinear absorption coefficient of -3.9×10^{-10} mW^{-1}, and demonstrated the potential to substitute semiconductor saturable absorber mirrors, especially in the NIR region.[50]

If there is a field that has received a great deal of attention in recent years, it is energy. In this sense, 2D materials, and 2D-Pn in particular, have several properties that make them especially interesting. With respect to energy conversion, Sb has been employed as electrocatalysts for water splitting, with special focus on hydrogen evolution reaction (HER) in acid media.[23] For that, Sb-based materials obtained through LPE using different solvents and wet-ball milling processes have been obtained. Interestingly, we discovered that the preparation protocol triggers different oxidation degrees on the final

Open Access Article. Published on 21 April 2023. Downloaded on 5/10/2026 2:30:36 PM.
This article is licensed under a Creative Commons Attribution-NonCommercial 3.0 Unported Licence.

materials, which results in marked differences in terms of HER performance. Indeed, the higher the surface oxidation, the better obtained overpotential values, and Tafel slopes. This is particularly the case for the samples prepared using BuOH, which exhibited better exfoliation and anisotropic ratio yielding a large number of edges and electroactive sites (Fig. 10G–K). This behaviour seems to also be related to the irreversible formation of superficial antimony oxides.[42]

Last but not least, concerning energy storage, 2D-Pn have been postulated as excellent electrode materials for Lithium Ion Batteries (LIBs) and Sodium-Ion Batteries (SIBs) because their 2D structures enable fast ion diffusion and easy accessibility to redox sites.[124–126] It is also very important to mention their potential as anode material for alloy-based batteries. Indeed, heavy Pn show higher theoretical specific and volumetric capacities compared to graphite, the most widely employed anode material to date.[127,128] Their ability to generate reversible alloys is the key point for their use, permitting fast charge/discharge mechanisms. Moreover, 2D-Pn exhibit lower volumetric expansion, decreasing the technological problems that arise during anode charge.[129] Along this front, we carried out a thorough analysis of the sodiation process of the solid-state synthesis and the structure of the resulting intercalated bP/sodium phase, establishing the relevant parameters that lead to a successful sodiation. This solid-state protocol reveals the thermodynamically preferred range for the bulk formation of the intercalated phase, which consists of alternating Na-filled and empty layers as well as small areas of stage 1 intercalated layers (Fig. 10L). This work opens a door towards a large-scale synthesis of Na-bPIC, one of the most promising materials for SIBs.

From the point of view of the biomedical application, the rich chemical diversity of Pn play a very interesting role, making each of these 2D materials suitable for complementary applications.[130–133] For instance, phosphorene exhibits great ROS scavenger behavior and its degradation is effective in the treatment of neurodegenerative diseases like Parkinson, ELA or Alzheimer.[131,134–136] Conversely, antimonene ability to produce ROS combined with its great photothermal conversion efficiency (PTCE) can be exploited in cancer therapy to induce cellular toxicity and tumor ablation.[121,137,138] Arsenene was proved having antiproliferative effects on different cancer cells, especially on promyelotic leukemia cells.[139–141] Moreover, bismuthene could be used in therapies against antibiotic-resistant bacteria, owing to its antimicrobial properties.[130,142–145]

5. Summary and outlook

Throughout the group 15 the anisotropy decreases with increasing atomic number mainly due to the strong influence of the lone pairs, which facilitate the charge distribution between layers resulting in a more substantial interlayer interaction than that described by simple vdW forces. This is the reason why the preparation of isolated few to single-layer pnictogens is challenging and has remained elusive until today. 2D-pnictogens have been demonstrated to be feasible by employing different top-down approaches: (i) Micromechanical exfoliation (μME), in which few to single layers are peeled off of bulk bP, arsenic or antimony using a piece of tape. However, this approach doesn't work for bismuth. This method provides the highest quality crystals, but with a low yield. (ii) Liquid phase exfoliation (LPE), where layers are obtained inducing a shearing force by sonication of bulk pnictogens in different solvents allowing for an inexpensive and scalable production of FL bP, As, Sb and Bi. Indeed, LPE has been successfully developed for both bP and Sb, and for As and Bi the published protocols are far from presenting the same quality as their predecessors being oxidation or poor morphological control the main challenges to overcome. Whereas As and Sb lead to moderately large sheets with random morphologies, Bi undergoes a downsizing process together with exfoliation into relatively thick nanosheets. Other approaches like the bottom-up epitaxial growth methods, or CVD synthesis, despite being very promising, are still largely unexplored due to their complexity and low yield. In any case, the easy generation of large area SL-pnictogens remains elusive and we believe it should be one of the most active research fronts in the next few years.

Undoubtedly, one of the most important aspects in the future applications of 2D-Pn is the control over nanomaterials morphology. In this regard, it is particularly inspiring a recent achievement from Howard and coworkers, which showed the controlled synthesis of phosphorene nanoribbons (PNRs),[51] predicted to combine flexibility with unidirectional properties of one-dimensional materials together with high-surface area and electron-confinement effects.[74,146] PNRs were obtained after lithium intercalation of bP, and in a sequent article the group demonstrated the potential of these materials in inverted perovskite solar cells, drastically improving the devices performance. Furthermore, in the PNRs the electronic properties strongly depend on the morphology and width,[5] as well as the number of layers. For instance, in the case of bP, while bulk material has a direct bandgap (*ca.* 1.5 eV), NRs exhibit an indirect band gap that could be semiconductor or metallic depending on the structure.[75,146] Thus, we envision the isolation of a great variety on single- and few-layers pnictogen nanomaterials byway using heavy Pn intercalated with alkaline metals in a similar manner. Moreover, in the particular case of Bi, these exotic morphologies could give place to additional surface states of importance in topological insulators.[147] Nonetheless, as demonstrated for bP, the alkali metals intercalation approach could help to overcome the difficult problem of exfoliation of heavy pnictogens, as well as represent an innovative method for their covalent functionalization. Indeed, we believe that the preparation of large, high-quality monolayer 2D-pnictogens will be tackled by means of new advances in the field of alkali-metal intercalation as well as novel molecular bottom-up approaches. This will bring new horizons to the implementation of bP-based technologies, and in the development of novel pnictogen-based heterostructures with potential, among others, in (opto)electronics and spintronic applications, as long as the environmental stability is maximised by suitable functionalization.

 This journal is © The Royal Society of Chemistry 2023

Open Access Article. Published on 21 April 2023. Downloaded on 5/10/2026 2:30:36 PM.
This article is licensed under a Creative Commons Attribution-NonCommercial 3.0 Unported Licence.

Although the covalent chemistry of 2D materials has been extensively investigated in recent years, its transfer to 2D-Pn is not obvious due to its marked chemical reactivity. Indeed, bP functionalization already lived a quiet development, but heavy pnictogens haven't experienced a similar situation. Their semimetallic and metallic character is the main limitation to their covalent chemistry. One possibility for the covalent functionalization of Sb consists of exploiting the hydroxyl group formed during exfoliation, as reported by Xie and coworkers.[118] This could open the door to an approach similar to that shown by the chemistry of graphene oxide, where the functional groups on the surface were employed for further functionalization, without extra modification of the main material structure. Organic chemistry is rich in examples of –OH functionalization, thus reactions with strong electrophiles could be considered as functionalization pathways. Moreover, this approach could be common to the heavy pnictogens, anticipated by a controlled oxidation of the material to introduce reaction sites. On the other hand, the direct covalent functionalization of the neat element constituting the material remains an open challenge, and its development could pave the way for an innovative control of Pn properties, as well as a useful tool for the synthesis of covalent hybrid materials. Considering the large number of published contributions on the synthesis of antimony and bismuth chalcogenides (S, Se and Te), this objective could be pursued by analysing the organometallic chemistry of molecules containing S and Se, as it was developed for gold nanoparticles by using thiol and selenide derivatives.[148] Similarly, these groups could interact with lone pairs of As, Sb and Bi to form covalent interactions with the 2D structure. In a like manner to bP and other 2D materials, the surface functionalization will lead to punctual modification of the oxidation state of the functionalized atoms, as well as inducing lattice-strain on the Pn surface, consequently affecting their electronic and optical properties.[149] These effects are yet unknown and represent a completely open field. In this sense, we believe DFT calculations can help experimental researchers, predicting the effect of the described modification on Pn properties, guiding the synthetic efforts in a rational way.[150] Not of secondary importance, chemical functionalization could open the doors to the development of new functional materials and hybrids, including 2D–2D heterostructures, with a wide range of applications in electronics, nanomedicine and optics.

Finally, one of the aspects that highlights the importance of the chemical approach is the large limitations in the production of heavy 2D-Pn, which makes bottom-up approaches the only solution. In particular wet-chemistry methods like the recently developed colloidal approach hold great promise for the large-scale fabrication of high-quality 2D-Pn compatible with applications in electronics and beyond. Along this front, some works reported the preparation of 2D hexagonal crystals of Sb and Bi, however, further work should be done in order to precisely control the surface oxidation, size, thickness, and morphology. The great amount of reports based on Bi nanoentities demonstrate the feasibility of colloidal synthesis for general Pn production, providing a plethora of chemical precursors, solvents and conditions to work on it. Most of these reports present the synthesis of spherical nanoparticles,[151–156] but also in some cases other morphologies such as nanocubes,[67] nanowires,[67] nanohexagons,[157] faceted,[158] and ribbons,[72] among others. Nevertheless, considering the intrinsic anisotropy of the Pn structures, in-plane chemical bonds *vs.* out-of-plane interlayer interactions, soft chemical methods appear as the most proper ones to achieve a fine tuning of the morphological aspects. For instance, considering gold as an example, anisotropic growth can be promoted by the so-called seed-mediated growth. In this process, the formation of 2D systems would take place by the reduction of metal precursors on top of already formed small seeds. Then, the presence of the indicated shape-directing agents (metal ions, halides, organic compounds, surfactants) will drive the rest of the work.[159] Additionally, the compatibility of colloidal synthesis approaches with organometallic chemistry of Pn(III) cations in the initial reaction mixture could represent a pathway for the production of hybrids (either non-covalent or with covalent functionalization) in a one-pot straightforward procedure.

Summarising, as the preparation of large, monolayer 2D-pnictogens remains an open challenge, we are convinced that the future scientific and technological development of 2D-pnictogens will depend on the success of the new bottom-up methods, and specially in the colloidal routes. Likewise, we anticipate that two fields of research related to 2D-Pn will experience significant growth in the coming years: energy storage and biomedicine. Concerning the former, antimonene and bismuthene exhibit great potential as anode materials for both lithium- and sodium-ion batteries, even surpassing graphene, mainly due to the fast ion diffusion through their layers and the ability to intercalate alkali metals, something particularly relevant in the case of sodium. This pronounced chemical reactivity of 2D-Pn may be particularly beneficial in the case of biomedical applications, showing great potential for cancer therapy, theranostics, drug delivery systems, photothermal agents, or biosensing devices, to mention a few.

Overall, we hope that this feature article serves to highlight the importance of chemistry in the development of these emerging materials as well as to encourage further research on 2D pnictogens, opening the door for the development of exciting applications.

Conflicts of interest

The authors declare no conflict of interest.

Acknowledgements

This work has been supported by the European Union (ERC-2018-StG 804110-2D-PnictoChem), the Spanish MICINN (PID2019-111742GA-I00, PDC2022-133997-I00, TED2021-131347B-I00 and Excellence Unit María de Maeztu CEX2019-000919-M), the Generalitat Valenciana (CIDEGENT/2018/001), the Universitat de València and HUP/IIS La Fe (VLC-BIOMED AP2022-27).

Open Access Article. Published on 21 April 2023. Downloaded on 5/10/2026 2:30:36 PM.
This article is licensed under a Creative Commons Attribution-NonCommercial 3.0 Unported Licence.

M. A. L. acknowledges the Generalitat Valenciana for a post-doctoral fellowship (CIAPOS/2021/255).

References

1 K. S. Novoselov, A. K. Geim, S. V. Morozov, D. Jiang, Y. Zhang, S. V. Dubonos, I. V. Grigorieva and A. A. Firsov, *Science*, 2004, **306**, 666–669.
2 L. Li, Y. Yu, G. J. Ye, Q. Ge, X. Ou, H. Wu, D. Feng, X. H. Chen and Y. Zhang, *Nat. Nanotechnol.*, 2014, **9**, 372–377.
3 P. W. Bridgman, *J. Am. Chem. Soc.*, 1914, **36**, 1344–1363.
4 R. Hultgren, N. S. Gingrich and B. E. Warren, *J. Chem. Phys.*, 1935, **3**, 351.
5 F. Ersan, D. Kecik, V. O. Özçelik, Y. Kadioglu, O. Ü. Aktürk, E. Durgun, E. Aktürk and S. Ciraci, *Appl. Phys. Rev.*, 2019, **6**, 021308.
6 C. Backes, T. M. Higgins, A. Kelly, C. Boland, A. Harvey, D. Hanlon and J. N. Coleman, *Chem. Mater.*, 2017, **29**, 243–255.
7 Y. Zhang, L. Zhang and C. Zhou, *Acc. Chem. Res.*, 2013, **46**, 2329–2339.
8 R. F. Service, *Science*, 2015, **348**, 490–492.
9 N. Antonatos, H. Ghodrati and Z. Sofer, *Appl. Mater. Today*, 2020, **18**, 100502.
10 G. S. Girolami, *J. Chem. Educ.*, 2009, **86**, 1200.
11 V. Lloret, M. Á. Rivero-Crespo, J. A. Vidal-Moya, S. Wild, A. Doménech-Carbó, B. S. J. Heller, S. Shin, H.-P. Steinrück, F. Maier, F. Hauke, M. Varela, A. Hirsch, A. Leyva-Pérez and G. Abellán, *Nat. Commun.*, 2019, **10**, 509.
12 J. Sturala, Z. Sofer and M. Pumera, *Angew. Chem., Int. Ed.*, 2019, **58**, 7551–7557.
13 G. Abellán, V. Lloret, U. Mundloch, M. Marcia, C. Neiss, A. Görling, M. Varela, F. Hauke and A. Hirsch, *Angew. Chem., Int. Ed.*, 2016, **55**, 14557–14562.
14 J. M. Lipshultz, G. Li and A. T. Radosevich, *J. Am. Chem. Soc.*, 2021, **143**, 1699–1721.
15 D. Hanlon, C. Backes, E. Doherty, C. S. Cucinotta, N. C. Berner, C. Boland, K. Lee, A. Harvey, P. Lynch, Z. Gholamvand, S. Zhang, K. Wang, G. Moynihan, A. Pokle, Q. M. Ramasse, N. McEvoy, W. J. Blau, J. Wang, G. Abellan, F. Hauke, A. Hirsch, S. Sanvito, D. D. O'Regan, G. S. Duesberg, V. Nicolosi and J. N. Coleman, *Nat. Commun.*, 2015, **6**, 8563.
16 M. Fickert, M. Assebban, J. Canet-Ferrer and G. Abellán, *2D Mater.*, 2020, **8**, 015018.
17 Q. Wang and D. O'Hare, *Chem. Rev.*, 2012, **112**, 4124–4155.
18 R. Ma and T. Sasaki, *Acc. Chem. Res.*, 2015, **48**, 136–143.
19 J. Yu, Q. Wang, D. O'Hare and L. Sun, *Chem. Soc. Rev.*, 2017, **46**, 5950–5974.
20 R. C. Sahoo, S. Moolayadukkam, S. Thomas, M. Asle Zaeem and H. S. S. R. Matte, *Appl. Surf. Sci.*, 2021, **541**, 148270.
21 S. Zhang, Z. Yan, Y. Li, Z. Chen and H. Zeng, *Angew. Chem.*, 2015, **127**, 3155–3158.
22 S. Zhang, M. Xie, F. Li, Z. Yan, Y. Li, E. Kan, W. Liu, Z. Chen and H. Zeng, *Angew. Chem., Int. Ed.*, 2016, **55**, 1666–1669.
23 R. Gusmão, Z. Sofer, D. Bouša and M. Pumera, *Angew. Chem., Int. Ed.*, 2017, **56**, 14417–14422.
24 J. R. Brent, N. Savjani, E. A. Lewis, S. J. Haigh, D. J. Lewis and P. O'Brien, *Chem. Commun.*, 2014, **50**, 13338–13341.
25 C. Gibaja, D. Rodriguez-San-Miguel, P. Ares, J. Gómez-Herrero, M. Varela, R. Gillen, J. Maultzsch, F. Hauke, A. Hirsch, G. Abellán and F. Zamora, *Angew. Chem., Int. Ed.*, 2016, **55**, 14345–14349.
26 A. H. Woomer, T. W. Farnsworth, J. Hu, R. A. Wells, C. L. Donley and S. C. Warren, *ACS Nano*, 2015, **9**, 8869–8884.
27 M. B. Erande, S. R. Suryawanshi, M. A. More and D. J. Late, *Eur. J. Inorg. Chem.*, 2015, 3102–3107.
28 M. B. Erande, M. S. Pawar and D. J. Late, *ACS Appl. Mater. Interfaces*, 2016, **8**, 11548–11556.
29 A. Ambrosi, Z. Sofer and M. Pumera, *Angew. Chem., Int. Ed.*, 2017, **56**, 10443–10445.
30 J. B. Smith, D. Hagaman and H.-F. Ji, *Nanotechnology*, 2016, **27**, 215602.
31 Z. Yang, J. Hao, S. Yuan, S. Lin, H. M. Yau, J. Dai and S. P. Lau, *Adv. Mater.*, 2015, **27**, 3748–3754.
32 B. Tian, B. Tian, B. Smith, M. C. Scott, Q. Lei, R. Hua, Y. Tian and Y. Liu, *Proc. Natl. Acad. Sci. U. S. A.*, 2018, **115**, 4345–4350.
33 Y. Hu, J. Liang, Y. Xia, C. Zhao, M. Jiang, J. Ma, Z. Tie and Z. Jin, *Small*, 2022, **18**, 2104556.
34 L. Li, D. Zhang, M. Cao, J. Deng, X. Ji and Q. Wang, *J. Mater. Chem. C*, 2020, **8**, 9464–9475.
35 S. Kuriakose, S. K. Jain, S. A. Tawfik, M. J. S. Spencer, B. J. Murdoch, M. Singh, F. Rahman, E. L. H. Mayes, M. Y. Taha, R. T. Ako, V. Bansal, T. Ahmed, S. Sriram, M. Bhaskaran, S. Balendhran and S. Walia, *Adv. Mater. Interfaces*, 2020, **7**, 2001678.
36 Q. Wu and Y. J. Song, *Chem. Commun.*, 2018, **54**, 9671–9674.
37 C. Backes, D. Campi, B. M. Szydlowska, K. Synnatschke, E. Ojala, F. Rashvand, A. Harvey, A. Griffin, Z. Sofer, N. Marzari, J. N. Coleman and D. D. O'Regan, *ACS Nano*, 2019, **13**, 7050–7061.
38 J. Zhang, S. Ye, Y. Sun, F. Zhou, J. Song and J. Qu, *Nanoscale*, 2020, **12**, 20945–20951.
39 L. Peng, S. Ye, J. Song and J. Qu, *Angew. Chem., Int. Ed.*, 2019, **58**, 9891–9896.
40 I. Torres, M. Alcaraz, R. Sanchis-Gual, J. A. Carrasco, M. Fickert, M. Assebban, C. Gibaja, C. Dolle, D. A. Aldave, C. Gómez-Navarro, E. Salagre, E. G. Michel, M. Varela, J. Gómez-Herrero, G. Abellán and F. Zamora, *Adv. Funct. Mater.*, 2021, **31**, 2101616.
41 H. Liu, A. T. Neal, Z. Zhu, Z. Luo, X. Xu, D. Tománek and P. D. Ye, *ACS Nano*, 2014, **8**, 4033–4041.
42 C. Gibaja, M. Assebban, I. Torres, M. Fickert, R. Sanchis-Gual, I. Brotons, W. S. Paz, J. J. Palacios, E. G. Michel, G. Abellán and F. Zamora, *J. Mater. Chem. A*, 2019, **7**, 22475–22486.
43 P. Ares, F. Aguilar-Galindo, D. Rodríguez-San-Miguel, D. A. Aldave, S. Díaz-Tendero, M. Alcamí, F. Martín, J. Gómez-Herrero and F. Zamora, *Adv. Mater.*, 2016, **28**, 6332–6336.
44 V. Lloret, M. Á. Rivero-Crespo, J. A. Vidal-Moya, S. Wild, A. Doménech-Carbó, B. S. J. Heller, S. Shin, H.-P. Steinrück, F. Maier, F. Hauke, M. Varela, A. Hirsch, A. Leyva-Pérez and G. Abellán, *Nat. Commun.*, 2019, **10**, 509.
45 G. Abellán, S. Wild, V. Lloret, N. Scheuschner, R. Gillen, U. Mundloch, J. Maultzsch, M. Varela, F. Hauke and A. Hirsch, *J. Am. Chem. Soc.*, 2017, **139**, 10432–10440.
46 S. M. Beladi-Mousavi, A. M. Pourrahimi, Z. Sofer and M. Pumera, *Adv. Funct. Mater.*, 2019, **29**, 1807004.
47 Z.-H. Qi, Y. Hu, Z. Jin and J. Ma, *Phys. Chem. Chem. Phys.*, 2019, **21**, 12087–12090.
48 Y. Chen, C. Chen, R. Kealhofer, H. Liu, Z. Yuan, L. Jiang, J. Suh, J. Park, C. Ko, H. S. Choe, J. Avila, M. Zhong, Z. Wei, J. Li, S. Li, H. Gao, Y. Liu, J. Analytis, Q. Xia, M. C. Asensio and J. Wu, *Adv. Mater.*, 2018, **30**, 1800754.
49 L. Lu, Z. Liang, L. Wu, Y. Chen, Y. Song, S. C. Dhanabalan, J. S. Ponraj, B. Dong, Y. Xiang, F. Xing, D. Fan and H. Zhang, *Laser Photonics Rev.*, 2018, **12**, 1700221.
50 Q.-Q. Yang, R.-T. Liu, C. Huang, Y.-F. Huang, L.-F. Gao, B. Sun, Z.-P. Huang, L. Zhang, C.-X. Hu, Z.-Q. Zhang, C.-L. Sun, Q. Wang, Y.-L. Tang and H.-L. Zhang, *Nanoscale*, 2018, **10**, 21106–21115.
51 M. C. Watts, L. Picco, F. S. Russell-Pavier, P. L. Cullen, T. S. Miller, S. P. Bartuś, O. D. Payton, N. T. Skipper, V. Tileli and C. A. Howard, *Nature*, 2019, **568**, 216–220.
52 A. Pal, S. Saha, S. Kumar Maji, M. Kundu and A. Kundu, *Adv. Mater. Lett.*, 2012, **3**, 177–180.
53 A. Subastri, V. Arun, P. Sharma, E. Preedia babu, A. Suyavaran, S. Nithyananthan, G. M. Alshammari, B. Aristatile, V. Dharuman and C. Thirunavukkarasu, *Chem.-Biol. Interact.*, 2018, **295**, 73–83.
54 P. Vishnoi, M. Mazumder, S. K. Pati and C. N. R. Rao, *New J. Chem.*, 2018, **42**, 14091–14095.
55 B. Zhou, J.-M. Hong and J.-J. Zhu, *Mater. Lett.*, 2005, **59**, 3081–3084.
56 A. Houdayer, R. Schneider, D. Billaud, J. Lambert and J. Ghanbaja, *Mater. Chem. Phys.*, 2007, **101**, 404–409.
57 N. Mntungwa, M. D. Khan, S. Mlowe and N. Revaprasadu, *Mater. Lett.*, 2015, **145**, 239–242.
58 W. Li, P. Rong, K. Yang, P. Huang, K. Sun and X. Chen, *Biomaterials*, 2015, **45**, 18–26.
59 W. Tao, X. Ji, X. Xu, M. A. Islam, Z. Li, S. Chen, P. E. Saw, H. Zhang, Z. Bharwani, Z. Guo, J. Shi and O. C. Farokhzad, *Angew. Chem., Int. Ed.*, 2017, **56**, 11896–11900.
60 S. T. Dibaba, R. Caputo, W. Xi, J. Z. Zhang, R. Wei, Q. Zhang, J. Zhang, W. Ren and L. Sun, *ACS Appl. Mater. Interfaces*, 2019, **11**, 48290–48299.
61 Y. Gao, C. Lin, K. Zhang, W. Zhou, S. Guo, W. Liu, L. Jiang, S. Zhang and H. Zeng, *Adv. Funct. Mater.*, 2021, **31**, 2102766.

 This journal is © The Royal Society of Chemistry 2023

Open Access Article. Published on 21 April 2023. Downloaded on 5/10/2026 2:30:36 PM.
This article is licensed under a Creative Commons Attribution-NonCommercial 3.0 Unported Licence.

62 M. Yarema, M. V. Kovalenko, G. Hesser, D. V. Talapin and W. Heiss, *J. Am. Chem. Soc.*, 2010, **132**, 15158–15159.
63 C. J. Tang, G. H. Li, X. C. Dou, Y. X. Zhang and L. Li, *J. Phys. Chem. C*, 2009, **113**, 5422–5427.
64 H. Winter, E. Christopher-Allison, A. L. Brown and A. M. Goforth, *Nanotechnology*, 2018, **29**, 155603.
65 H. Bi, F. He, Y. Dong, D. Yang, Y. Dai, L. Xu, R. Lv, S. Gai, P. Yang and J. Lin, *Chem. Mater.*, 2018, **30**, 3301–3307.
66 D. Ma, J. Zhao, Y. Zhao, X. Hao, L. Li, L. Zhang, Y. Lu and C. Yu, *Colloids Surf., A*, 2012, **395**, 276–283.
67 W. Z. Wang, B. Poudel, Y. Ma and Z. F. Ren, *J. Phys. Chem. B*, 2006, **110**, 25702–25706.
68 I. Torres, A. M. Villa-Manso, M. Revenga-Parra, C. Gutiérrez-Sánchez, D. A. Aldave, E. Salagre, E. G. Michel, M. Varela, J. Gómez-Herrero, E. Lorenzo, F. Pariente and F. Zamora, *Appl. Mater. Today*, 2022, **26**, 101360.
69 M. Ozhukil Valappil, A. Ganguly, J. Benson, V. K. Pillai, S. Alwarappan and P. Papakonstantinou, *RSC Adv.*, 2020, **10**, 43585–43591.
70 O. H. Basyouni, M. Abdelfatah, M. E. El-Khouly, T. Mohamed, A. El-Shaer and W. Ismail, *J. Alloys Compd.*, 2021, **882**, 160766.
71 S. Mourdikoudis, N. Antonatos, V. Mazánek, I. Marek and Z. Sofer, *Inorg. Chem.*, 2022, **61**, 5524–5538.
72 F. Wang, R. Tang, H. Yu, P. C. Gibbons and W. E. Buhro, *Chem. Mater.*, 2008, **20**, 3656–3662.
73 G. Abellán, C. Neiss, V. Lloret, S. Wild, J. C. Chacón-Torres, K. Werbach, F. Fedi, H. Shiozawa, A. Görling, H. Peterlik, T. Pichler, F. Hauke and A. Hirsch, *Angew. Chem., Int. Ed.*, 2017, **56**, 15267–15273.
74 S. Lee, F. Yang, J. Suh, S. Yang, Y. Lee, G. Li, H. Sung Choe, A. Suslu, Y. Chen, C. Ko, J. Park, K. Liu, J. Li, K. Hippalgaonkar, J. J. Urban, S. Tongay and J. Wu, *Nat. Commun.*, 2015, **6**, 8573.
75 J. Zhang, H. J. Liu, L. Cheng, J. Wei, J. H. Liang, D. D. Fan, J. Shi, X. F. Tang and Q. J. Zhang, *Sci. Rep.*, 2014, **4**, 6452.
76 T. J. Macdonald, A. J. Clancy, W. Xu, Z. Jiang, C.-T. Lin, L. Mohan, T. Du, D. D. Tune, L. Lanzetta, G. Min, T. Webb, A. Ashoka, R. Pandya, V. Tileli, M. A. McLachlan, J. R. Durrant, S. A. Haque and C. A. Howard, *J. Am. Chem. Soc.*, 2021, **143**, 21549–21559.
77 Y. Xia, Y. Xiong, B. Lim and S. E. Skrabalak, *Angew. Chem., Int. Ed.*, 2009, **48**, 60–103.
78 T. S. Rodrigues, M. Zhao, T.-H. Yang, K. D. Gilroy, A. G. M. da Silva, P. H. C. Camargo and Y. Xia, *Chem. – Eur. J.*, 2018, **24**, 16944–16963.
79 S. Mourdikoudis and Z. Sofer, *CrystEngComm*, 2021, **23**, 7876–7898.
80 J. O. Island, G. A. Steele, H. S. J. van der Zant and A. Castellanos-Gomez, *2D Mater.*, 2015, **2**, 011002.
81 A. Castellanos-Gomez, L. Vicarelli, E. Prada, J. O. Island, K. L. Narasimha-Acharya, S. I. Blanter, D. J. Groenendijk, M. Buscema, G. A. Steele, J. V. Alvarez, H. W. Zandbergen, J. J. Palacios and H. S. J. van der Zant, *2D Mater.*, 2014, **1**, 025001.
82 Y. Huang, J. Qiao, K. He, S. Bliznakov, E. Sutter, X. Chen, D. Luo, F. Meng, D. Su, J. Decker, W. Ji, R. S. Ruoff and P. Sutter, *Chem. Mater.*, 2016, **28**, 8330–8339.
83 M. A. Lucherelli, X. Qian, P. Weston, M. Eredia, W. Zhu, P. Samorì, H. Gao, A. Bianco and A. von dem Bussche, *Adv. Mater.*, 2021, 2103137.
84 A. Favron, E. Gaufrès, F. Fossard, A.-L. Phaneuf-L'Heureux, N. Y.-W. Tang, P. L. Lévesque, A. Loiseau, R. Leonelli, S. Francoeur and R. Martel, *Nat. Mater.*, 2015, **14**, 826–832.
85 S. Wild, V. Lloret, V. Vega-Mayoral, D. Vella, E. Nuin, M. Siebert, M. Koleśnik-Gray, M. Löffler, K. J. J. Mayrhofer, C. Gadermaier, V. Krstić, F. Hauke, G. Abellán and A. Hirsch, *RSC Adv.*, 2019, **9**, 3570–3576.
86 M. Tejeda-Serrano, V. Lloret, B. G. Márkus, F. Simon, F. Hauke, A. Hirsch, A. Doménech-Carbó, G. Abellán and A. Leyva-Pérez, *ChemCatChem*, 2020, **12**, 2226–2232.
87 G. Abellán, P. Ares, S. Wild, E. Nuin, C. Neiss, D. R.-S. Miguel, P. Segovia, C. Gibaja, E. G. Michel, A. Görling, F. Hauke, J. Gómez-Herrero, A. Hirsch and F. Zamora, *Angew. Chem., Int. Ed.*, 2017, **56**, 14389–14394.
88 S. Wolff, R. Gillen, M. Assebban, G. Abellán and J. Maultzsch, *Phys. Rev. Lett.*, 2020, **124**, 126101.
89 M. Assebban, C. Gibaja, M. Fickert, I. Torres, E. Weinreich, S. Wolff, R. Gillen, J. Maultzsch, M. Varela, S. Tan Jun Rong, K. P. Loh, E. G. Michel, F. Zamora and G. Abellán, *2D Mater.*, 2020, **7**, 025039.
90 F. Bonaccorso, L. Colombo, G. Yu, M. Stoller, V. Tozzini, A. C. Ferrari, R. S. Ruoff and V. Pellegrini, *Science*, 2015, **347**, 1246501.
91 Q. Tang, Z. Zhou and Z. Chen, *Nanoscale*, 2013, **5**, 4541.
92 M. A. Lucherelli, Y. Yu, G. Reina, G. Abellán, E. Miyako and A. Bianco, *Angew. Chem.*, 2020, **132**, 14138–14143.
93 A. Mitrović, G. Abellán and A. Hirsch, *RSC Adv.*, 2021, **11**, 26093–26101.
94 S. Presolski and M. Pumera, *Mater. Today*, 2016, **19**, 140–145.
95 C. Xing, L. Liu, D. Fan, Z. Peng and H. Zhang, *FlatChem*, 2019, **13**, 8–24.
96 H. Ghodrati, N. Antonatos and Z. Sofer, *Small*, 2019, **15**, 1903495.
97 V. V. Chaban, E. E. Fileti and O. V. Prezhdo, *ACS Nano*, 2017, **11**, 6459–6466.
98 S. Walia, S. Balendhran, T. Ahmed, M. Singh, C. El-Badawi, M. D. Brennan, P. Weerathunge, Md. N. Karim, F. Rahman, A. Rassell, J. Duckworth, R. Ramanathan, G. E. Collis, C. J. Lobo, M. Toth, J. C. Kotsakidis, B. Weber, M. Fuhrer, J. M. Dominguez-Vera, M. J. S. Spencer, I. Aharonovich, S. Sriram, M. Bhaskaran and V. Bansal, *Adv. Mater.*, 2017, **29**, 1700152.
99 V. Lloret, E. Nuin, M. Kohring, S. Wild, M. Löffler, C. Neiss, M. Krieger, F. Hauke, A. Görling, H. B. Weber, G. Abellán and A. Hirsch, *Adv. Mater. Interfaces*, 2020, **7**, 2001290.
100 Y. Du, L. Yang, H. Zhou and P. D. Ye, *IEEE Electron Device Lett.*, 2016, **37**, 429–432.
101 P. Vishnoi, S. Rajesh, S. Manjunatha, A. Bandyopadhyay, M. Barua, S. K. Pati and C. N. R. Rao, *Chem. Phys. Chem.*, 2017, **18**, 2985–2989.
102 R. Gusmão, Z. Sofer and M. Pumera, *ACS Nano*, 2018, **12**, 5666–5673.
103 Z. Guo, S. Chen, Z. Wang, Z. Yang, F. Liu, Y. Xu, J. Wang, Y. Yi, H. Zhang, L. Liao, P. K. Chu and X.-F. Yu, *Adv. Mater.*, 2017, **29**, 1703811.
104 D. Tofan, Y. Sakazaki, K. L. Walz Mitra, R. Peng, S. Lee, M. Li and A. Velian, *Angew. Chem., Int. Ed.*, 2021, **60**, 8329–8336.
105 X. Liu, L. Xiao, J. Weng, Q. Xu, W. Li, C. Zhao, J. Xu and Y. Zhao, *Sci. Adv.*, 2020, **6**, eabb4359.
106 T. García-Mendiola, C. Gutiérrez-Sánchez, C. Gibaja, I. Torres, C. Busó-Rogero, F. Pariente, J. Solera, Z. Razavifar, J. J. Palacios, F. Zamora and E. Lorenzo, *ACS Appl. Nano Mater.*, 2020, **3**, 3625–3633.
107 M. Barua, M. Monis Ayyub, S. Acharya and C. N. R. Rao, *Nanoscale*, 2022, **14**, 13834–13843.
108 C. R. Ryder, J. D. Wood, S. A. Wells, Y. Yang, D. Jariwala, T. J. Marks, G. C. Schatz and M. C. Hersam, *Nat. Chem.*, 2016, **8**, 597–602.
109 Y. Liu, M. Chen and S. Yang, *InfoMat*, 2021, **3**, 231–251.
110 G. Abellán, M. Schirowski, K. F. Edelthalhammer, M. Fickert, K. Werbach, H. Peterlik, F. Hauke and A. Hirsch, *J. Am. Chem. Soc.*, 2017, **139**, 5175–5182.
111 M. A. Lucherelli, J. Raya, K. F. Edelthalhammer, F. Hauke, A. Hirsch, G. Abellán and A. Bianco, *Chem. – Eur. J.*, 2019, **25**, 13218–13223.
112 S. Wild, M. Fickert, A. Mitrovic, V. Lloret, C. Neiss, J. A. Vidal-Moya, M. Á. Rivero-Crespo, A. Leyva-Pérez, K. Werbach, H. Peterlik, M. Grabau, H. Wittkämper, C. Papp, H. Steinrück, T. Pichler, A. Görling, F. Hauke, G. Abellán and A. Hirsch, *Angew. Chem., Int. Ed.*, 2019, **58**, 5763–5768.
113 K. Werbach, C. Neiss, A. Müllner, G. Abellán, D. Setman, V. Lloret, S. Wild, F. Hauke, T. Pichler, A. Hirsch and H. Peterlik, *Batteries Supercaps*, 2021, **4**, 1304–1309.
114 S. Wild, X. T. Dinh, H. Maid, F. Hauke, G. Abellán and A. Hirsch, *Angew. Chem., Int. Ed.*, 2020, **59**, 20230–20234.
115 A. Mitrović, S. Wild, V. Lloret, M. Fickert, M. Assebban, B. G. Márkus, F. Simon, F. Hauke, G. Abellán and A. Hirsch, *Chem. – Eur. J.*, 2021, **27**, 3361–3366.
116 J. Sturala, A. Ambrosi, Z. Sofer and M. Pumera, *Angew. Chem., Int. Ed.*, 2018, **57**, 14837–14840.
117 M. M. Ayyub, M. Barua, S. Acharya and C. N. R. Rao, *Small*, 2022, **18**, 2203554.
118 F. Xing, J. Wang, Z. Wang, Y. Li, X. Gou, H. Zhang, S. Zhou, J. Zhao and Z. Xie, *ACS Appl. Mater. Interfaces*, 2021, **13**, 897–903.
119 E. Palacios, J. A. Rodríguez-Velamazán, M. Evangelisti, G. J. McIntyre, G. Lorusso, D. Visser, L. J. de Jongh and L. A. Boatner, *Phys. Rev. B: Condens. Matter Mater. Phys.*, 2014, **90**, 214423.
120 G. Pizzi, M. Gibertini, E. Dib, N. Marzari, G. Iannaccone and G. Fiori, *Nat. Commun.*, 2016, **7**, 12585.

Open Access Article. Published on 21 April 2023. Downloaded on 5/10/2026 2:30:36 PM.
This article is licensed under a Creative Commons Attribution-NonCommercial 3.0 Unported Licence.

121 J. Wu, X. Cai, G. R. Williams, Z. Meng, W. Zou, L. Yao, B. Hu, Y. Chen and Y. Zheng, *Bioact. Mater.*, 2022, **10**, 295–305.
122 J. Gu, Z. Du, C. Zhang, J. Ma, B. Li and S. Yang, *Adv. Energy Mater.*, 2017, **7**, 1700447.
123 S. Wang, W. Wang and G. Zhao, *Phys. Chem. Chem. Phys.*, 2016, **18**, 31217–31222.
124 J. Pang, A. Bachmatiuk, Y. Yin, B. Trzebicka, L. Zhao, L. Fu, R. G. Mendes, T. Gemming, Z. Liu and M. H. Rummeli, *Adv. Energy Mater.*, 2018, **8**, 1702093.
125 P. Ares, J. J. Palacios, G. Abellán, J. Gómez-Herrero and F. Zamora, *Adv. Mater.*, 2018, **30**, 1703771.
126 X. Liu, S. Zhang, S. Guo, B. Cai, S. A. Yang, F. Shan, M. Pumera and H. Zeng, *Chem. Soc. Rev.*, 2020, **49**, 263–285.
127 S. M. Beladi-Mousavi and M. Pumera, *Chem. Soc. Rev.*, 2018, **47**, 6964–6989.
128 M. Ai, J. Sun, Z. Li, H. Liang and C. Liu, *J. Phys. Chem. C*, 2021, **125**, 11391–11401.
129 J. Zhou, J. Chen, M. Chen, J. Wang, X. Liu, B. Wei, Z. Wang, J. Li, L. Gu, Q. Zhang, H. Wang and L. Guo, *Adv. Mater.*, 2019, **31**, 1807874.
130 D. M. Griffith, H. Li, M. V. Werrett, P. C. Andrews and H. Sun, *Chem. Soc. Rev.*, 2021, **50**, 12037.
131 M. Luo, T. Fan, Y. Zhou, H. Zhang and L. Mei, *Adv. Funct. Mater.*, 2019, **29**, 1808306.
132 V. Urbanová and M. Pumera, *Nanoscale*, 2019, **11**, 15770–15782.
133 C. Liu, J. Shin, S. Son, Y. Choe, N. Farokhzad, Z. Tang, Y. Xiao, N. Kong, T. Xie, J. S. Kim and W. Tao, *Chem. Soc. Rev.*, 2021, **50**, 2260–2279.
134 X. Liu, B. Gaihre, M. N. George, Y. Li, M. Tilton, M. J. Yaszemski and L. Lu, *Biomater. Sci.*, 2021, **9**, 2768–2803.
135 Y. Li, Z. Du, X. Liu, M. Ma, D. Yu, Y. Lu, J. Ren and X. Qu, *Small*, 2019, **15**, 1901116.
136 W. Chen, J. Ouyang, X. Yi, Y. Xu, C. Niu, W. Zhang, L. Wang, J. Sheng, L. Deng, Y. Liu and S. Guo, *Adv. Mater.*, 2018, **30**, 1703458.
137 W. Tao, X. Ji, X. Zhu, L. Li, J. Wang, Y. Zhang, P. E. Saw, W. Li, N. Kong, M. A. Islam, T. Gan, X. Zeng, H. Zhang, M. Mahmoudi, G. J. Tearney and O. C. Farokhzad, *Adv. Mater.*, 2018, **30**, 1802061.
138 Y. Duo, Y. Huang, W. Liang, R. Yuan, Y. Li, T. Chen and H. Zhang, *Adv. Funct. Mater.*, 2020, **30**, 1906010.
139 X. Wang, Y. Hu, J. Mo, J. Zhang, Z. Wang, W. Wei, H. Li, Y. Xu, J. Ma, J. Zhao, Z. Jin and Z. Guo, *Angew. Chem., Int. Ed.*, 2020, **59**, 5151–5158.
140 N. Kong, H. Zhang, C. Feng, C. Liu, Y. Xiao, X. Zhang, L. Mei, J. S. Kim, W. Tao and X. Ji, *Nat. Commun.*, 2021, **12**, 4777.
141 N. F. Rosli, C. C. Mayorga-Martinez, A. C. Fisher, O. Alduhaish, R. D. Webster and M. Pumera, *Appl. Mater. Today*, 2020, **21**, 100819.
142 J. A. Salvador, S. A. Figueiredo, R. M. Pinto and S. M. Silvestre, *Future Med. Chem.*, 2012, **4**, 1495–1523.
143 H. Song, J. Wang, B. Xiong, J. Hu, P. Zeng, X. Liu and H. Liang, *Angew. Chem., Int. Ed.*, 2022, **61**, e202117679.
144 L. Bai, W. Yi, J. Chen, B. Wang, Y. Tian, P. Zhang, X. Cheng, J. Si, X. Hou and J. Hou, *ACS Appl. Mater. Interfaces*, 2022, **14**, 25050–25064.
145 Y. Wang, W. Feng, M. Chang, J. Yang, Y. Guo, L. Ding, L. Yu, H. Huang, Y. Chen and J. Shi, *Adv. Funct. Mater.*, 2021, **31**, 2005093.
146 H. Guo, N. Lu, J. Dai, X. Wu and X. C. Zeng, *J. Phys. Chem. C*, 2014, **118**, 14051–14059.
147 C. Sabater, D. Gosálbez-Martínez, J. Fernández-Rossier, J. G. Rodrigo, C. Untiedt and J. J. Palacios, *Phys. Rev. Lett.*, 2013, **110**, 176802.
148 C. K. Yee, A. Ulman, J. D. Ruiz, A. Parikh, H. White and M. Rafailovich, *Langmuir*, 2003, **19**, 9450–9458.
149 M. Zhao, X. Zhang and L. Li, *Sci. Rep.*, 2015, **5**, 16108.
150 A.-X. Zhang, J.-T. Liu, S.-D. Guo and H.-C. Li, *Phys. Chem. Chem. Phys.*, 2017, **19**, 14520–14526.
151 S. C. Warren, A. C. Jackson, Z. D. Cater-Cyker, F. J. DiSalvo and U. Wiesner, *J. Am. Chem. Soc.*, 2007, **129**, 10072–10073.
152 D. Leng, T. Wang, Y. Li, Z. Huang, H. Wang, Y. Wan, X. Pei and J. Wang, *Inorg. Chem.*, 2021, **60**, 17258–17267.
153 B. Wei, X. Zhang, C. Zhang, Y. Jiang, Y.-Y. Fu, C. Yu, S.-K. Sun and X.-P. Yan, *ACS Appl. Mater. Interfaces*, 2016, **8**, 12720–12726.
154 Z. Wang, C. Jiang, R. Huang, H. Peng and X. Tang, *J. Phys. Chem. C*, 2014, **118**, 1155–1160.
155 J. S. Son, K. Park, M.-K. Han, C. Kang, S.-G. Park, J.-H. Kim, W. Kim, S.-J. Kim and T. Hyeon, *Angew. Chem., Int. Ed.*, 2011, **50**, 1363–1366.
156 Y. Wang and Y. Xia, *Nano Lett.*, 2004, **4**, 2047–2050.
157 Z. Zhang, M. Chi, G. M. Veith, P. Zhang, D. A. Lutterman, J. Rosenthal, S. H. Overbury, S. Dai and H. Zhu, *ACS Catal.*, 2016, **6**, 6255–6264.
158 N. Yu, Z. Wang, J. Zhang, Z. Liu, B. Zhu, J. Yu, M. Zhu, C. Peng and Z. Chen, *Biomaterials*, 2018, **161**, 279–291.
159 L. M. Liz-Marzán and M. Grzelczak, *Science*, 2017, **356**, 1120–1121.

 This journal is © The Royal Society of Chemistry 2023